

Quantum Coherent Transport of 1D Ballistic States in Second-Order Topological Insulator Bi_4Br_4

Jules Lefeuvre,^{1,*} Masaru Kobayashi,² Gilles Patriarche,³ Nathaniel Findling,³ David Troadec,⁴ Meydi Ferrier,¹ Sophie Guéron,¹ H el ene Bouchiat,¹ Takao Sasagawa,² and Richard Deblock^{1,†}

¹*Universit e Paris-Saclay, CNRS, Laboratoire de Physique des Solides, 91405, Orsay, France.*

²*Materials and Structures Laboratory, Institute of Science Tokyo, Yokohama, Japan.*

³*Universit e Paris-Saclay, CNRS, Centre de Nanosciences et de Nanotechnologies, 91120, Palaiseau, France.*

⁴*Universit e de Lille, CNRS, Institut d'Electronique, de Micro electronique et de Nanotechnologie, 59652, Villeneuve d'Ascq, France*

We investigate quantum transport in micrometer-sized single crystals of Bi_4Br_4 , a material predicted to be a second-order topological insulator. 1D topological states with long phase coherence times are revealed via the modulation of quantum interference with magnetic field and gate voltage. In particular, we demonstrate the existence of Aharonov-Bohm interference between 1D ballistic states several micrometers long, that we identify as phase-coherent hinge modes on neighboring step edges at the crystal surface. These Aharonov-Bohm oscillations are made possible by a disordered phase-coherent contact region, the existence of which is confirmed by scanning transmission electron microscopy combined with energy-dispersive X-ray spectroscopy (STEM-EDX) of FIB lamellae. Their coherent nature modulates the transmission of the 1D edge states, leading to weak antilocalization and universal conductance fluctuations with surprisingly large characteristic fields and a strongly anisotropic behavior. These complementary experimental results provide a comprehensive, coherent description of quantum transport in Bi_4Br_4 , and establish the material as a second-order topological insulator with topologically protected 1D ballistic states.

I. INTRODUCTION

An important recent achievement in condensed matter physics is the discovery of a new class of materials, topological insulators (TIs), whose bulk is insulating, while the boundaries are conducting [1–3]. In particular, the 1D edges of 2DTIs realize the quantum spin hall (QSH) state [4, 5], where current is carried dissipationlessly by two counterpropagating ballistic channels with opposite spins, forming a helical edge state. This opens many possibilities, ranging from dissipationless charge and spin transport at room temperature, to new avenues for quantum computing. Among the recent additions to the TI classification, second order topological insulators (SOTIs) [6, 7] are n -dimensional crystals exhibiting $(n - 2)$ -dimensional topological states. In particular, 3D SOTIs have insulating bulk and surfaces, but topologically protected, one-dimensional helical “hinge” states. 1D helical states have been evidenced in several systems in 2D such as HgTe quantum wells [8], monolayer WTe_2 [9, 10], or TaIrTe_4 [13] and in 3D systems such as crystalline bismuth [11, 12]. Unfortunately, the expected topological protection has turned out to be less robust than anticipated, notably due to the existence of conduction in the bulk and surface, or charge puddles [14]. This complicates the fundamental study of the edge states, and motivates the search for different TIs with a reduced contribution of the nontopological bulk states. Among newly discovered TIs, Bi_4Br_4 appears to be a very promising

material, with a large bulk gap ($\gtrsim 200$ meV) [15–21], and strong experimental indications of a SOTI character [22–25].

This material, which in its α form has a bilayer structure of chains oriented along the crystal's b direction [Fig. 1(a) and 1(b)], has indeed been predicted to show the QSH state for the monolayer [15, 16] and the multilayer has been classified as a SOTI [17–21, 23, 26–29]. The SOTI character in the multilayer case results from the coupling of helical edge states upon stacking of 2D monolayers, leading to gapped side surfaces with a gap of the order of 30 meV. On a perfect crystal, only two helical states located at hinges remain uncoupled, which location depends on the parity of the number of layers.

The band structure of Bi_4Br_4 has been probed by angle-resolved photoemission spectroscopy (ARPES) [22–24] and micro-ARPES [25]. This latter work confirmed the existence of gapped lateral surfaces, with a gap ranging from 28 to 40 meV, and resolved their spin texture, indicating a spin polarization perpendicular to the direction of the chains. In addition, optical pump-probe microscopy at room temperature revealed a relatively long carrier lifetime for boundary states attributed to their linear dispersion relation [26]. Lastly, conducting hinge states have been probed by STM [23, 27–29] up to room temperature, on mono- and few-layers-high step edges. These states are gapped by a magnetic field perpendicular to chains with a Land e factor of 53, indicating a spin quantization axis along the b axis, in stark contrast to the spin polarization of bulk [20] and lateral surface states [25].

With regard to electronic transport, experiments carried out on macroscopic samples indicate that the temperature dependence of resistivity is close to that of a

* jules.lefeuvre@universite-paris-saclay.fr

† richard.deblock@universite-paris-saclay.fr

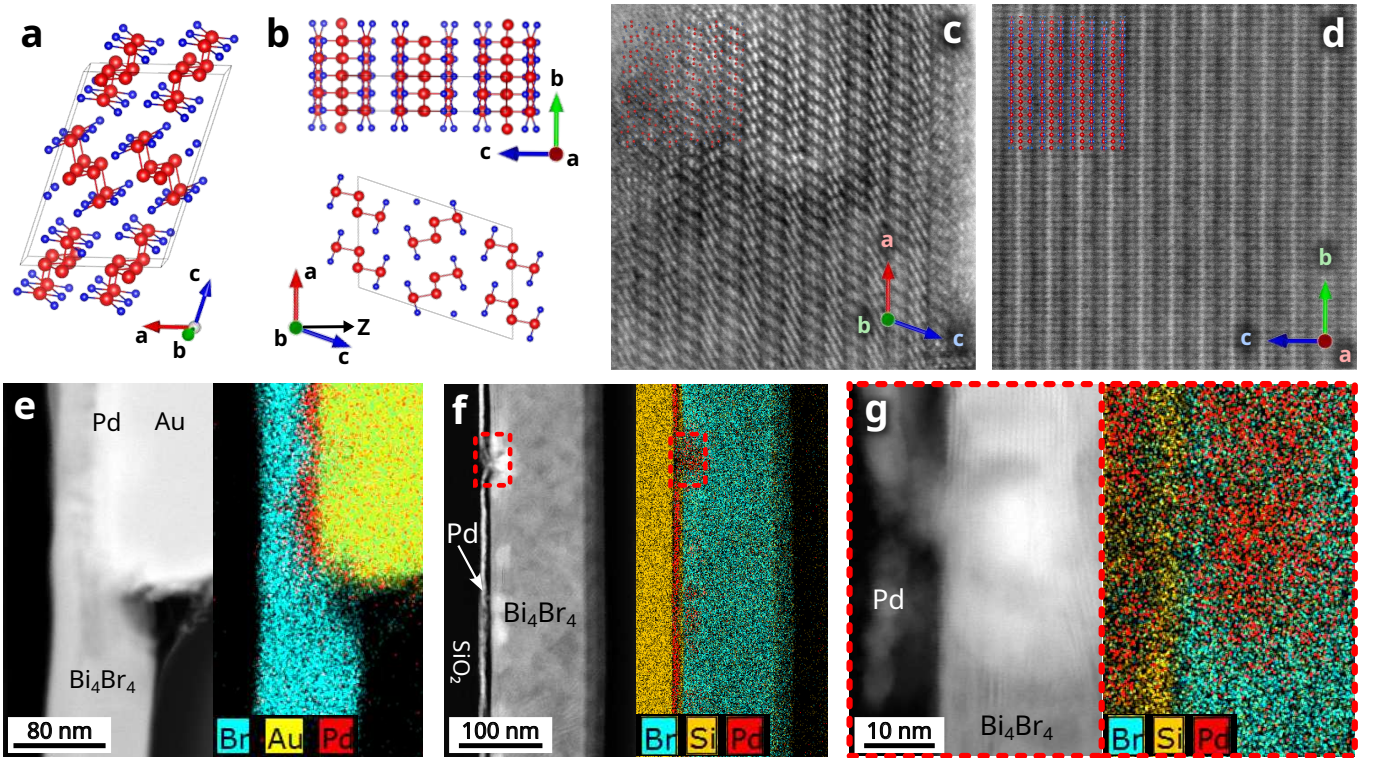


FIG. 1. Structure of Bi_4Br_4 crystals far from and in the contact region. (a) Crystalline structure of Bi_4Br_4 and crystal orientation. Bi atoms are figured in red, and Br in blue. (b) Structure of Bi_4Br_4 along the a and b axis. The Z direction, perpendicular to the (a,b) plane of the flakes, is indicated. (c) High-resolution high-angle-annular dark-field (HAADF) STEM images of FIB lamellae of contacted Bi_4Br_4 flakes obtained along the b direction, away from the contact area. The expected crystalline structure is superimposed on the picture. The agreement between theoretical and real atoms positions is excellent. (d) Similar image along the a direction. (e) Contact region of Au/Pd (100 nm/7 nm) top-contacted electrodes, showing crystal damage both under and away from the electrode. The EDX analysis (right image) shows a diffusion of Bi in the Pd and, to a lesser extent, in the Au layers. The spurious Si signal in the gold electrode is due to the proximity of a fluorescence band of Au with the Si $K\alpha$. (f) Contact region for 7-nm-thick Pd electrodes placed below the Bi_4Br_4 flakes. Diffusion of Pd in the crystal is also visible. (g) Enlargement of the area denoted by the red dashed rectangle in (f), which evidence disordered contact regions of size around 100 nm.

semiconductor below 50 K and often shows a local maximum around 200 K [22, 23, 30–34]. It has been proposed that the former results from either competition between bulk and hinge states [22, 30], or the appearance of a charge density wave [32, 33] or a variable-range hopping induced by Br vacancies [34], while the 200 K feature is attributed to a Lifshitz transition [23, 30]. At low temperature, macroscopic samples exhibit weak localization or weak antilocalization depending on the field orientation [35, 36]. High-pressure experiments found a metal-insulator transition that can even lead to a superconducting state at pressures above 3.8 GPa [33]. By probing micrometer-size crystals obtained by exfoliation, several temperature behaviors were obtained: a nearly temperature-independent resistivity for relatively long flakes [37], a gate tunable resistance attributed to competition of bulk and surface conduction [38], or a thermal activation of bulk carriers [39]. This latter reference demonstrated an Aharonov-Bohm effect associated to quantum interference of coherent hinge states around

single lateral surfaces in four- and six-layer flakes.

In the present work, we study quantum transport in micrometer-sized Bi_4Br_4 flakes with thicknesses ranging from 50 to 150 nm. We find evidence of phase-coherent ballistic 1D states over several microns via the Aharonov-Bohm effect, as well as negative four-wire resistances. Interestingly, the samples also consistently display weak antilocalization and universal conductance fluctuations, which are staples of 2D coherent transport in the diffusive regime. These apparently conflicting observations can be reconciled by considering a small, coherent, but disordered region between the pristine crystal and the contact, which enables both interhinge coherence and anomalous 2D quantum interference. The existence of this region is confirmed by direct imaging and elemental analysis using STEM-EDX. While this contact regime prevents observation of the quantification of conductance generally expected in QSH systems, it provides extremely rich signatures of the underlying topological transport.

II. EXFOLIATION AND CONTACTING OF Bi_4Br_4 FLAKES

The Bi_4Br_4 crystals were synthesized by the chemical vapor transport method [22, 40]. The samples were exfoliated in a glove box under argon atmosphere with $\text{O}_2 < 0.2$ ppm and $\text{H}_2\text{O} < 5$ ppm. The exfoliation and transfer of micrometer-size Bi_4Br_4 flakes was done using PDMS stamps. We check with STEM imaging that the crystalline quality of the exfoliated flakes is preserved before any contacts is made (Sec. 1 in Supplemental Material [41]).

In order to contact the flakes we developed two strategies. The first one is based on contacts made on top of the flake. This is done by e-beam lithography, with low-temperature processes to preserve the quality of the flakes (PMMA resist baking below 100°C), and metal deposition in an e-beam evaporator after argon ion beam etching. Different contact materials were tried. The best results were obtained with palladium (Pd). The samples are thus contacted by Pd(7 nm)/Au(100 nm) electrodes; this leads to $\text{k}\Omega$ two-wire resistances at room temperature. However, this method damages the crystal under the contacts and exposes the flakes to organic solvents and ambient air during the e-beam lithography and lift-off processes. To avoid these problems, we also tried contacting the flakes by transferring them onto predefined metallic electrodes, fabricated by e-beam and optical lithography, with e-beam metal deposition. The Bi_4Br_4 flakes are then pressed onto the electrodes in Ar atmosphere. During this process, we found that heating the transfer stage to 80°C produced Ohmic contacts more reliably. The best results were obtained, as in the case of contacts on top, with palladium electrodes and also yields two-wire resistances in the $\text{k}\Omega$ range.

To understand the nature of the contact region between Pd electrodes and Bi_4Br_4 flakes, we produced FIB lamellae of the region of the contacts, as well as slices away from the contacts and analyzed them in a STEM. The results are presented in Fig. 1. Sections taken far from the contacts show excellent crystalline quality, even after exposure to ambient air [Fig. 1(c) and 1(d)]. By contrast, for both contacting schemes, the contact regions are disordered, with Pd/Bi interdiffusion, and have a typical size of approximately 100 nm.

III. ANISOTROPIC ELECTRONIC TRANSPORT IN Bi_4Br_4 FLAKES

We have performed electronic transport measurements on more than ten samples. In the following, we focus on four samples. One, denoted \mathcal{L} , is a flake with six contacts [top contacts with Pd(7 nm)/Au(100 nm) electrodes], thus defining five segments, with length ranging from 1 to $5\ \mu\text{m}$. The flake has a total length of $30\ \mu\text{m}$, a width of $2.1\ \mu\text{m}$ and a thickness of around 100 nm [Fig. 4(a)]. The flake is deposited on a doped silicon substrate,

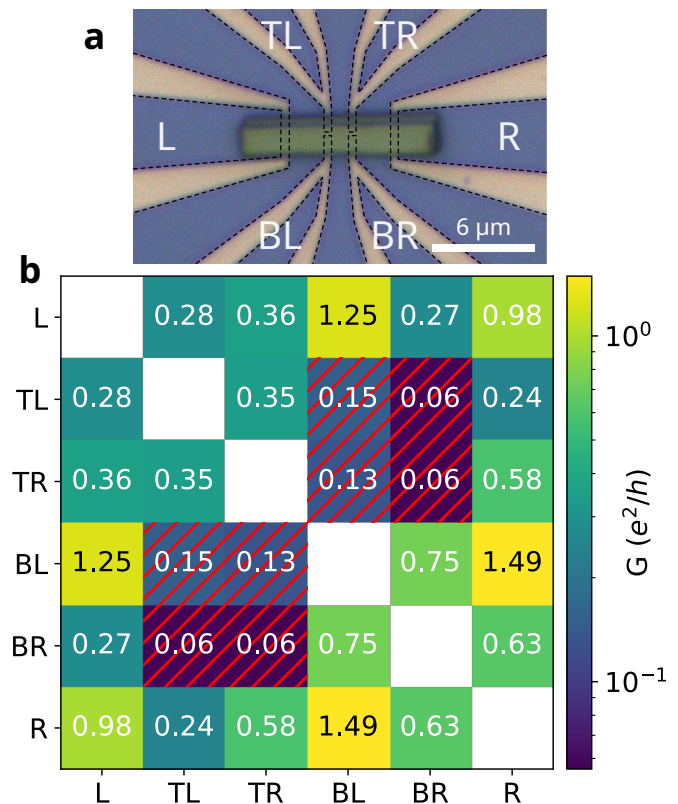


FIG. 2. Anisotropic transport in Bi_4Br_4 sample \mathcal{H}_1 at 10 mK and under a 500 nA dc bias. (a) Optical picture of sample \mathcal{H}_1 with labeling of the electrodes. (b) Conductance matrix of sample \mathcal{H}_1 . The conductances are small in the transverse direction (a axis of the crystal), highlighted by red hatching, and much higher, by a factor 10, in the longitudinal direction (b axis of the crystal).

which serves as a back gate, covered by 500 nm of oxide.

We also discuss three samples with a Hall bar geometry. Sample \mathcal{H}_1 , shown in Fig. 2(a), is a flake deposited on top of Ti(5 nm)/Au(10 nm)/Pd(5 nm) contacts. Sample \mathcal{H}_3 has similar contacts, while sample \mathcal{H}_2 has Pd(7 nm)/Au(100 nm) contacts deposited from the top (Fig. 5 and Sec. 2 of Supplemental Material [41]).

All samples display four-wire resistance values in the $\text{k}\Omega$ range at room temperature that do not change significantly down to 10 K [Fig. 3(a)]. There is a sharp increase of resistance below 1 K, which we attribute to the mesoscopic nature of our sample rather than to the band structure (Sec. 7 of Supplemental Material [41]). The absence of a strong temperature dependence in our measurements contrasts with other works [22, 23, 30, 32–34, 38] and suggests that our samples are relatively clean, with a low density of doping defects, and, therefore, have a rather temperature-stable chemical potential. Moreover, the absence of a temperature-activated behavior across the whole temperature range suggests that the Fermi level lies at least 26 meV away from a bulk band edge, thus clearly in the bulk gap.

The four-wire resistances of the segments of sample \mathcal{L} do not increase proportionally to their lengths, which indicates that they are dominated by a contact resistance (Sec. 3 of Supplemental Material [41]). This can be explained by two competing scenarios: either a resistive interface between the Pd/Au contacts and well-conducting bulk or surface states, or ballistic conduction, likely due to hinge states. The variations in resistance from segment to segment can, thus, be explained either by fluctuations in interface quality or by differences in the number of edge modes contacted due to insulating resist residues under the electrodes.

In order to elucidate the flow of current inside the Hall bar devices, we use a formula derived in the context of graph theory [63, 64]:

$$\mathcal{G} = -2\mathcal{R}^{-1} + 2\frac{\mathcal{R}^{-1}\mathbf{u}\mathbf{u}^T\mathcal{R}^{-1}}{\mathbf{u}\mathcal{R}^{-1}\mathbf{u}^T} \quad (1)$$

which relates two quantities, the Laplacian matrix \mathcal{G} and the resistance distance matrix \mathcal{R} , with \mathbf{u} a vector with all coefficients equal to 1. Modeling the sample as a network of lumped resistances with nodes representing terminals, the resistance distance matrix \mathcal{R} contains the two-wire resistances between each possible pair of terminals of the resistance network. The Laplacian matrix \mathcal{G} has matrix elements $\mathcal{G}_{ij} = -G_{ij}$, with G_{ij} the discrete node-to-node conductances, and diagonal coefficients ensuring current conservation $\mathcal{G}_{ii} = \sum_{j \neq i} G_{ij}$. \mathcal{G} , thus, corresponds to the conductance matrix in the context of mesoscopic transport [65]. This result, therefore, provides a direct determination of the conductance matrix from simple resistance measurements [66].

The conductance matrix of \mathcal{H}_1 is given in Fig. 2(b) (see Sec. 2 in Supplemental Material [41] for samples \mathcal{H}_2 and \mathcal{H}_3). All contacts to the flake are doubled, so that the lead resistance can be removed for every two-wire configuration. We find a very anisotropic transport, with relatively high conductances, of the order of the conductance quantum, along the b direction of the crystal. Noticeably, the conduction along the a direction is consistently among the smallest in all of our devices, with conductances under $0.15 e^2/h$ for contacts 500 nm apart for \mathcal{H}_1 . Nonzero transverse conductances may result from residual interface resistances that are not eliminated by our measurement procedure.

Finally, we have carried out magnetotransport measurements (Fig. 3) on the same sample, which revealed an essentially symmetrical four-wire transverse resistance dominated by quantum interferences at low temperature (see the next section). The antisymmetrical fraction of the contribution to the magnetoresistance is extremely small, with no clear linear dependence in magnetic field, indicating the absence of Hall effect in the sample. Accordingly, the longitudinal resistance exhibits no Shubnikov-de Haas oscillations (Sec. 8 in Supplemental Material [41]), further demonstrating the absence of transverse transport.

These results are a striking demonstration that the

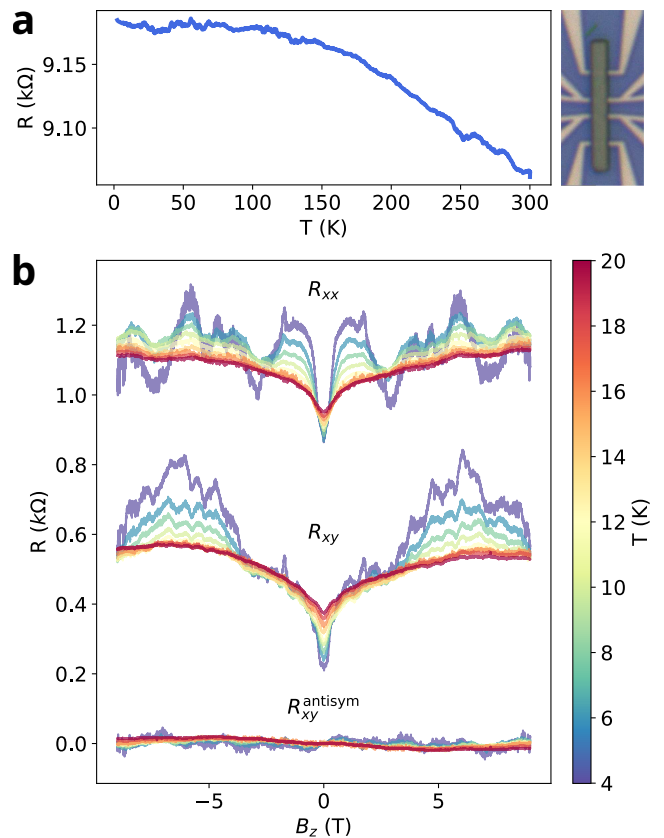


FIG. 3. Temperature dependence of electronic transport in Bi_4Br_4 . (a) Temperature dependence of a representative Bi_4Br_4 sample, measured in a physical property measurement system. A Savitzky-Golay filter was applied to the data to get rid of the high-frequency noise. Right: optical picture of the sample used for temperature dependence. (b) Longitudinal (R_{xx}) and transverse (R_{xy}) magnetoresistance at temperature between 4 (purple) and 20 K (red) for sample \mathcal{H}_1 . R_{xy}^{antisym} corresponds to the antisymmetric part of the transverse resistance and shows no Hall effect.

bulk and (001) surfaces are insulating. It suggests that conduction is either due to the lateral (100) surfaces or to 1D states along the b direction.

IV. LOW-TEMPERATURE QUANTUM TRANSPORT

At low temperature, the differential resistance of all samples exhibits a zero-bias peak, which cannot be attributed to self-heating (Sec. 7 of Supplemental Material [41]). Considering the linear regime, with a low excitation current, and for temperatures below 20 K, magnetoconductance has two main characteristics: a weak-antilocalization (WAL) peak at zero magnetic field, and sizable universal conductance fluctuations (UCFs) [Fig. 4(c) for sample \mathcal{L}].

The low-field WAL peaks are fitted using the Hikami-

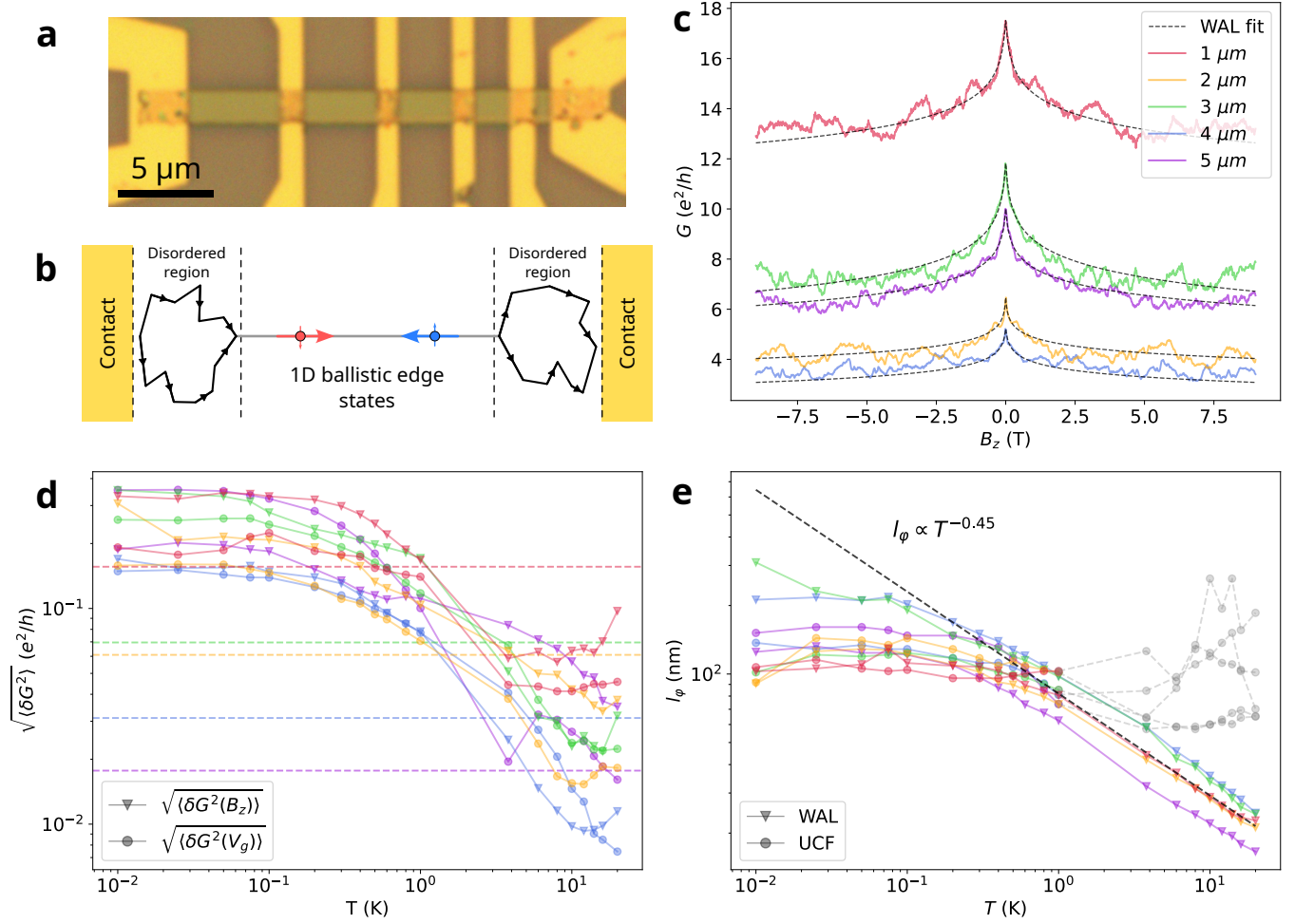


FIG. 4. Coherent quantum transport measurement in sample \mathcal{L} . (a) Optical image of sample \mathcal{L} . (b) Sketch of the different sample regions contributing to the quantum transport. (c) Magnetoconductance at 10 mK of all segments for an out-of-plane magnetic field. Correspondence between the segment and curve is indicated in the legend. The dashed line is a fit of the WAL component using formula (2). (d) Dependence of UCF amplitudes (in units of e^2/h) as a function of temperature. The amplitude is deduced from the gate dependence (round symbols) or the magnetic field dependence (triangle symbols) of the UCFs. The color code is the same as in (c). The horizontal dashed lines are the expected value of the UCF for a diffusive conductor of the same length and same α as the considered section if self-averaging is assumed. (e) l_φ extracted from both the UCFs (round symbols) and WAL (triangle symbols), showing a power-law dependence in temperature with exponent -0.45 . l_φ saturates for temperatures below 100 mK. The part of the curve in gray indicates the range of temperature where UCFs cannot be reliably extracted due to experimental noise.

Larkin-Nagaoka relation :

$$\delta G(B) = \frac{\alpha e^2}{2\pi h} \left[\Psi \left(\frac{1}{2} + \frac{\hbar}{4eBl_\varphi^2} \right) - \ln \left(\frac{\hbar}{4eBl_\varphi^2} \right) \right] \quad (2)$$

with Ψ the digamma function, B the magnetic field, l_φ the phase coherence length and α a prefactor corresponding to the number of independent channels in parallel [67, 68]. Equation (2) is valid for a 2D diffusive conductor in the limit of very strong spin-orbit coupling (spin-orbit length $l_{\text{SO}} \ll l_\varphi$). The fitting is done in the magnetic field range $[-1 \text{ T}, 1 \text{ T}]$ for temperatures under 2 K, and $[-3 \text{ T}, 3 \text{ T}]$ otherwise with two adjustable parameters : the prefactor α , which is kept constant for a given segment at all temperatures, and the phase coherence length l_φ .

Formula (2) gives an excellent agreement over the entire field range. This seems to indicate the absence of other contributions to the magnetoconductance. However, fits using the WAL expression in the case of quasi-1D conductors yielded both a poor agreement with the experimental data and inconsistent values for l_φ (Sec. 6 of Supplemental Material [41]). We find relatively short l_φ across all segments, between 100 nm and 200 nm at low temperatures [Fig. 4(e)] and values for α between 2 and 8, which suggests the existence of several uncorrelated electron paths in parallel [67, 69, 70].

We now turn to the analysis of the UCFs, which were measured as a function of magnetic field [Fig. 4(c)] and gate voltage (Sec. 3 of Supplemental Material [41]). The

UCFs exhibit a typical magnetic field scale, given by the half-width of the autocorrelation, which provides another determination of l_φ [71–73]. As shown in Fig. 4(e), these values are close to those extracted from WAL, except at temperatures above 1 K, for which the experimental noise outweighs the UCF signal. For all sections of sample \mathcal{L} , l_φ extracted from both WAL and UCFs follows a power-law dependence down to approximately 100 mK, below which it saturates. We find an exponent of -0.45 , consistent with the expected $-1/2$ for dephasing in 2D dominated by electron-electron interactions [67].

Despite l_φ being much shorter than the segment length, we find sizable fluctuation amplitudes with no systematic decrease with increasing segment length. We recall that UCF in diffusive conductors should decrease as the segment length extends beyond l_φ , due to self-averaging. By contrast, the absence of a systematic decrease in fluctuations amplitude with length [Fig. 4(d)] shows that the quantum interference we measure does not originate from a diffusive path within the flake.

Rather, we propose that diffuse transport occurs only in the damaged region near the contacts, roughly 100 nm in size as discussed above. Those diffusive regions are connected by 1D ballistic channels, up to $5 \mu\text{m}$ long, so that coherent transport occurs over up to $5 \mu\text{m}$. We conjecture that it is the transmission from contacts to ballistic channel that is modulated by quantum interference in the disordered regions. This is what leads to the absence of self-averaging and to the high field scale of UCF and WAL. This scenario was already pointed out in the context of the conductance of edge states in the integer quantum Hall effect [75] and is qualitatively reproduced by our numerical simulations [Fig. 8(a) and section 5 in Supplemental Material [41]].

To confirm this picture, we studied the dependence of quantum interference on magnetic field orientation. We performed magnetoconductance measurements on samples \mathcal{L} using a vector magnet, allowing it to apply magnetic fields in arbitrary directions up to 1 T. We present field cuts in three different planes : in-plane, longitudinal and transverse, all taken at 3.8 K to remove the contribution from conductance fluctuations, which complicates the analysis [Fig. 5(a)-5(c)]. The first two cuts clearly highlight a near absence of magnetoconductance along the b axis of the flake [X direction of Figs. 5(a) and 5(b)]. The longitudinal and transverse cuts reveal that the decrease of conductance with magnetic field is maximum for an out-of-plane field, leading an extended lobe in the polar plot in the perpendicular direction (indicated by the red lines in Fig. 5), demonstrating that the surface of diffusion essentially lies in the plane of the sample. This behavior, together with the absence of self-averaging of the UCFs, rules out diffusion on the sides surfaces of Bi_4Br_4 as the source of the observed quantum interferences.

In addition to the large out-of-plane magnetoconductance observed in the transverse cut, several devices con-

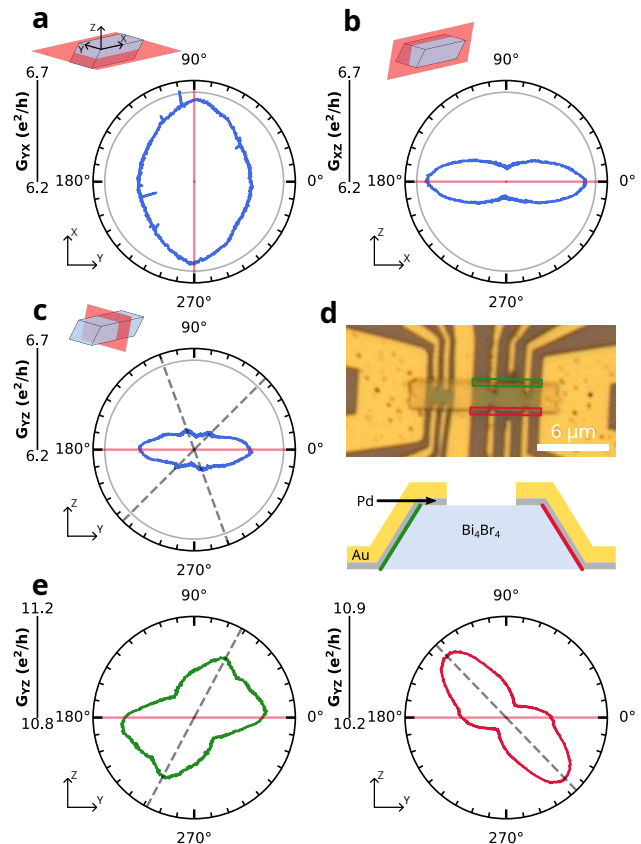


FIG. 5. (a)-(c) : Magnetoconductance anisotropy at 3.8 K for the $4\text{-}\mu\text{m}$ segment of sample \mathcal{L} . (a) Top : schematic image of the flake and the XY plane in which the magnetic field is applied. Bottom : variation of the conductance by sweeping the magnetic field angle in the XY plane, for a magnetic field modulus of 1 T. The angle 0° corresponds to a field aligned along the Y direction. Magnetoconductance is highest in the Y direction, defining an extended lobe in the perpendicular X direction, as indicated by the red line. (b) Similar data for a magnetic field in the XZ plane, showing a maximum magnetoconductance along the Z direction. (c) Similar data for a magnetic field in the YZ plane, showing a maximum magnetoconductance along the Z direction and side lobes, indicated by gray dashed lines, attributed to the geometry of the contacts (see the text). (d) Top : optical image of the sample \mathcal{H}_2 . Bottom : sketch of the cross section of the flake \mathcal{H}_2 . (e) Magnetoconductance with a magnetic field of 1 T in the YZ plane for lateral contacts indicated in (d) in green (left part) or red (right part). The direction of maximum magnetoconductance is not related to the crystalline orientation but rather to the geometry of the lateral contacts.

tacted from the top exhibit other lobes [gray dashed lines in Figs. 5(c), 5(f) and 5(g)] that are not related to any specific crystalline direction of Bi_4Br_4 . Rather, these axes correspond to the planes of the electrodes deposited on the lateral side of the flake. Indeed, the disordered region induced by the contacts follows the slope of the etched crystal, which defines the plane of diffusion for the WAL [Fig. 5(e)]. Moreover, for sample \mathcal{H}_2 , with a Hall bar geometry, we find that, for contacts on the

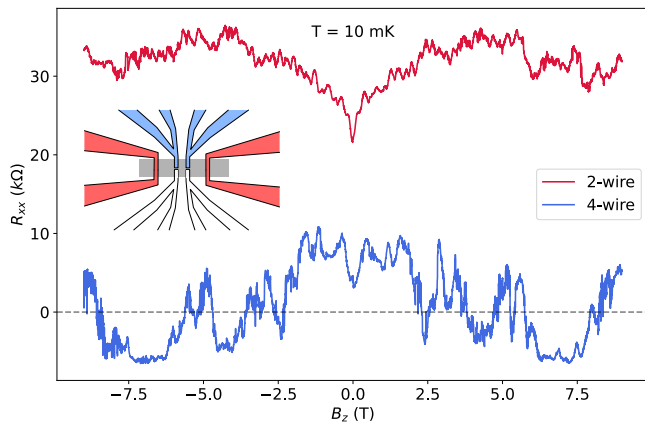


FIG. 6. Two- and four-wire longitudinal resistances of sample \mathcal{H}_1 as a function of magnetic field at $T = 10$ mK, measured with a 10 nA ac current. The four-wire measurement is negative in several field ranges. Inset : sample geometry with the Bi_4Br_4 flake in gray, current injection in red and voltage probes in blue. For the two-wire measurement, the voltage probes are the red wires.

side of the flakes, only one of the side lobes is present and that it is more prominent than the out-of-plane one. This confirms that each side lobe comes from one flank of the flake. In contrast, samples contacted from below showed only an out-of-plane magnetoconductance, confirming that the origin of the side lobes lies in the contact method.

In conclusion, magnetotransport at low temperature and its anisotropy with magnetic field orientation confirms that the regions determining the mesoscopic fluctuations are the diffusive contact regions, leading to a field-dependent transmission to 1D ballistic channels.

V. NEGATIVE FOUR-WIRE RESISTANCE

While the behavior of samples contacted from above and from below are similar on many aspects, there are a few clear differences. The first is the presence of a higher interface resistance for bottom contacts, and the second is the absence of a four-wire negative differential resistance in top-contacted samples.

Indeed, we observe negative four-wire resistance fluctuations that extend between -6 and 10 kΩ with a two-wire resistance of 20-35 kΩ for \mathcal{H}_1 (Fig. 6). This corresponds to a sizable fraction of the theoretical limit of $\pm R_{2\text{wires}}$, predicted for ballistic conduction measured with moderately invasive voltage probes [76]. Indeed, the two-wire resistance measured through the voltage probes indicated in blue in Fig. 6 is high (approximately 150 kΩ), which may indicate a weakly perturbative contact to the edge states that can favor the appearance of these negative fluctuations. Indeed, contacts from below may allow for the hinge states to be preserved to a certain extent, if they are not cut by a large Pd/Bi alloy region

(Fig. 1). We emphasize that this prediction of a four-wire negative differential resistance for ballistic systems has not been reported by many studies. Experiments on single-walled carbon nanotubes have found negative fluctuations reaching the theoretical limit [77], as well as measurements on high-mobility GaAs 2DEGs, which were observed only in a specific field range [78, 79]. Both of these experiments featured exceptionally clean systems with noninvasive voltage probes, which contrasts with the disorder induced at the contacts with Bi_4Br_4 . Therefore, this observation of negative differential resistance in our samples could be a consequence of the expected topological protection of hinge states against elastic disorder.

VI. AHARONOV-BOHM INTERFERENCE

In addition to the aperiodic UCFs and WAL displayed in the magnetoconductance, several samples also display periodic oscillations, leading to well-defined peaks in their Fourier transform (FFT).

In particular the longitudinal magnetoresistance of sample \mathcal{H}_1 shows a very clear periodicity of around 0.24 T at low temperatures leading to a FFT peak at 4 T^{-1} [Fig.7(a) and 7(c)]. Note that the periodicity of the oscillations does not depend on temperature but the amplitude does (Sec. 4 of Supplemental Material [41]). We interpret this as Aharonov-Bohm (AB) interference [80] between two 1D states of length $6 \mu\text{m}$ and separated by 2.7 nm, allowed by the partially coherent contact region, as confirmed by numerical simulations [Fig. 8(b) and Sec. 5 of Supplemental Material [41]]. One possible reason for this particularly clear signature of AB interference in this sample is the small separation between the lateral electrodes, which selects only a few channels that can carry current coherently across the flake without being interrupted by a contact [Fig.7(b)]. The good visibility of the AB oscillations is also favored by the small lateral distance between edge states, comparable to the mean free path in the diffusive contact [Sec. 5 of Supplemental Material [41]]. Besides, we find an exponential decay with temperature of the AB amplitude [inset in Fig. 7(c)]. This temperature behavior has been reported in quasi-1D ballistic rings [85], 3D topological insulators [81–83] and hinge state loops in thin MoTe_2 flakes [84]. This dependence is, however, at odds with the result of Hossain *et al.* [39] on thin flakes of Bi_4Br_4 , which instead exhibits a power-law dependence that is attributed to the extremely long, effectively temperature-independent, phase coherence length of edge states. The functional difference between the decay of the UCFs and AB oscillations with temperature in our samples suggests that their coherence is limited by distinct mechanisms. One would expect the amplitude of AB oscillations to be proportional to the probability of an electron trajectory to complete a loop without phase-breaking event $\exp(-P/l_\varphi)$, with P the perimeter of the closed trajectory [80]. The exponential decay of the peak amplitude in the FFT with tempera-

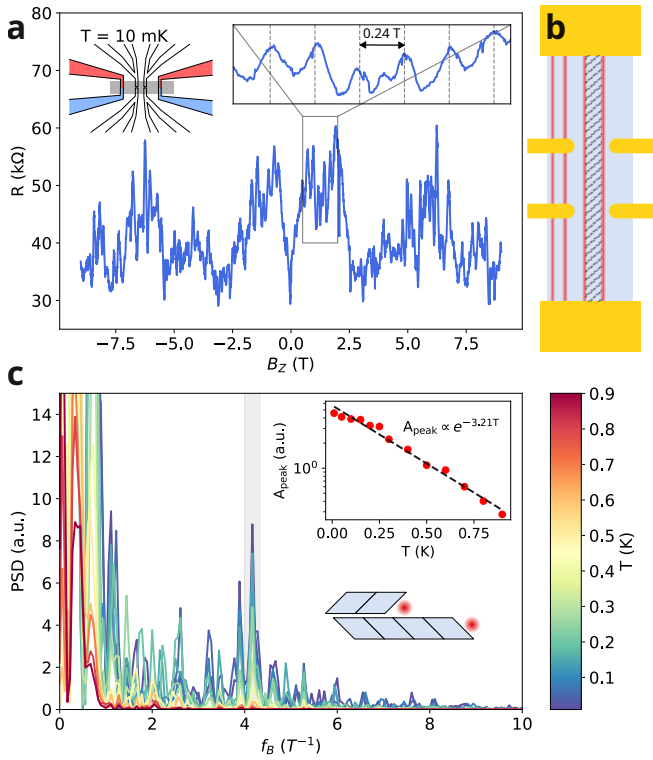


FIG. 7. Aharonov-Bohm effect of sample \mathcal{H}_1 . (a) Magnetoconductance at low temperature exhibiting periodic conductance oscillations, with a field period of 0.24 T. Left inset : configuration of the contacts used for current injection (red) and voltage probing (blue). Right inset : enlargement of a reduced field range. (b) Schematic picture of the Bi_4Br_4 flake (blue) with its contacts (yellow). The red lines represent 1D states, some of which are interrupted by lateral contacts. The two central 1D states delimit a surface (hatched area) defining the magnetic field periodicity of the AB effect. (c) Power spectral density of the magnetoconductance of sample \mathcal{H}_1 at different temperatures. The gray area indicates the peak corresponding to the observed conductance oscillations, taking into account an uncertainty of $\pm 20 \times 20 \text{ nm}^2$. Top inset : temperature dependence of the FFT peak area. It is consistent with an exponential decay with temperature, of exponent -3.21 . Bottom inset : schematic image of a cross section of Bi_4Br_4 exhibiting a configuration of edge states compatible with the observed AB periodicity. The blue diamonds represent individual crystalline unit cells and the red dots show the position of edge states.

ture, therefore, implies a $1/T$ dependence of the phase coherence length and taking $P = 12 \text{ }\mu\text{m}$, $l_\varphi = 3.7 \text{ }\mu\text{m}$ at 1 K. The fact that we can measure such a long phase coherence length implies that phase breaking occurs predominantly within the hinge states, so that the electron trajectories contributing the most to the AB effect do not explore the diffusive regions much, thanks to the very small separation between hinge states (2.7 nm). Our results emphasize the coherence of electronic transport in relatively long Bi_4Br_4 flakes.

Strikingly, for device \mathcal{L} , several of the FFT peaks cor-

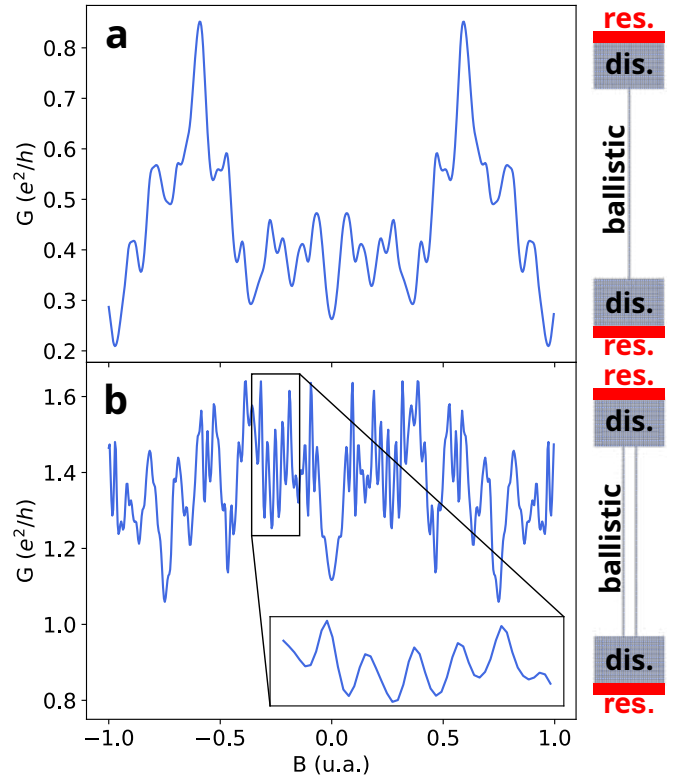


FIG. 8. Numerical simulations of the conductance of ballistic channels connected to reservoirs via a disordered coherent region realized with the KWANT software package [74]. (a) Case of a single ballistic channel showing WAL and UCFs. Right : tight binding network used to calculate the conductance (Sec. 5 of Supplemental Material [41]). The long, narrow region is the ballistic channel (noted ballistic). It is terminated by two diffusive coherent regions (noted dis.). The reservoirs are represented by the red rectangles (noted res.). (b) The same for two ballistic channels in parallel connected to reservoirs via a disordered coherent region. The conductance exhibits AB oscillations on top of WAL and UCFs. Right : corresponding tight binding network [41].

respond to a field scale proportional to the length of the considered segment. Hence, if the magnetic frequency is rescaled by the segment length [Fig. 9(b)], it is possible to identify some peaks in the FFT of different segments that correspond to the same rescaled magnetic frequency. We interpret this as AB interference around surfaces of fixed widths across each segment. We postulate that these oscillations originate from coherent 1D hinge states that extend over the entire length of the flake, which were subsequently divided into several segments by the fabricated contacts. Consequently, from segment to segment, there is a constant lateral separation between the hinge states, as illustrated in Fig. 9(a). In fact, the magnetic frequencies identified in the FFT spectrum can be related to some specific configurations of hinge states that are consistent with the crystalline structure of Bi_4Br_4 [Fig. 9(b)]. As the AB effect is visible for all segments, including the longest ones, the phase coherence length of the

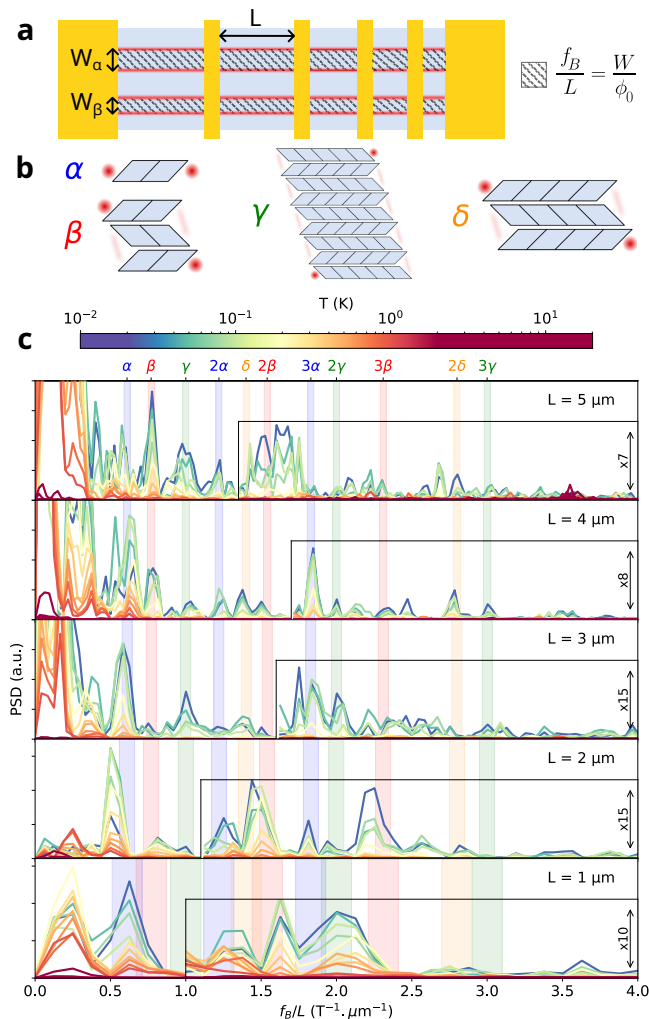


FIG. 9. AB effect in sample \mathcal{L} . (a) Schematic picture of the sample with the Bi_4Br_4 flake in blue and the contacts in yellow. The red lines represent 1D states, which are separated by a distance W and interrupted by the contacts. For a segment of length L , the AB magnetic field period is $\Phi_0/(WL)$, thus leading to a magnetic frequency $f_B = WL/\Phi_0$. (b) Hinge state configurations consistent with the observed AB peaks in the FFT [see (c)], where a blue diamond represents a crystalline unit cell and the red dots correspond to the hinge states. (c) Power spectral density of the magnetoconductance of the different segments of sample \mathcal{L} and for temperatures between 10 mK and 10 K, indicated by the color bar. The FFT frequencies are rescaled by the length of the corresponding segment. Shaded areas correspond to an uncertainty of $\pm 20 \times 20 \text{ nm}^2$ around a few identified peaks [see (b) and Sec. 4 of Supplemental Material [41]], denoted α (blue), β (red), γ (green) and δ (orange), and their harmonics.

edge states must be of the order of $5 \mu\text{m}$ or more. However, the limited phase coherence in the contact regions induces an upper cutoff to the lateral distance between 1D channels allowing for AB interferences, such that we do not observe peaks in the Fourier spectrum corresponding to distances greater than a few tens of nanometers.

Moreover, we attribute the absence of a clear magnetic field periodicity in the magnetoconductance signal to the multiplicity of frequencies present in the Fourier transform, which are due to the many 1D coherent channels of the flake that may interfere with each other. The temperature dependence of the identified peaks exhibits an exponential decay consistent with a $1/T$ dependence of phase coherence length and a value at 1 K similar to the one of sample \mathcal{H}_1 . Moreover the existence of AB interference in all segments of \mathcal{L} up to $5 \mu\text{m}$ is consistent with long phase coherence length.

VII. CONCLUSION

We have probed the electronic transport in micrometer-size Bi_4Br_4 flakes and have demonstrated a strongly anisotropic transport. We have highlighted two distinct types of contributions to low-temperature coherent transport and argue that they reveal the existence of long coherent 1D hinge states contacted to reservoirs via a small coherent disordered region. The first type of contribution yields universal conductance fluctuations and weak antilocalization, arising from phase coherence in the region close to the contacts, which modulates transmission through the 1D states. The second type of contribution is the periodic Aharonov-Bohm conductance oscillations due to interference between adjacent 1D coherent channels. We emphasize that both of these effects are due to the very nature of the contacts, which exhibit some phase coherence despite being rather invasive. These effects indicate that the 1D states are ballistic and coherent over several micrometers at low temperatures. The signature of the 1D ballistic states, located at step edges distributed at the surface of the Bi_4Br_4 crystal, and their interference are thus paradoxically revealed thanks to the coherent diffusive nature of the contact regions. It would be interesting to achieve the opposite limit of clean, crystal-preserving contacts in small samples with a reduced number of edge states, in order to access the conductance quantization regime. Also, the signature of the helical nature of these 1D states in multilayer samples remains to be demonstrated. Lastly, the use of superconducting contacts to enter the regime of proximity-induced superconductivity is of great interest, with expected perfect Andreev reflection, and would further enhance the potential of Bi_4Br_4 as a second-order topological insulator.

ACKNOWLEDGMENTS

The authors acknowledge B. Wieder, E. Gerber, T. Wakamura, M. Kociak, M. Aprili and J. Esteve for fruitful discussions, L. Bugaud's involvement in the initial steps of the project, and technical help from S. Autier-Laurent and R. Weil. This work was funded by JSPS KAKENHI (Grants No. 21H04652, No. 21K18181

and No. 21H05236), JST CREST (Grant No. JP-MJCR20B4), the French Renatech network, the CPER Hauts de France project IMITECH, the Métropole Européenne de Lille, and the European Union through the BALLISTOP ERC 66566 advanced grant.

DATA AVAILABILITY

The data that support the findings of this article are openly available [86].

-
- [1] M. Z. Hasan and C. L. Kane, Colloquium: Topological insulators, *Rev. Mod. Phys.* 82, 3045 (2010).
- [2] X.-L. Qi and S.-C. Zhang, Topological insulators and superconductors, *Rev. Mod. Phys.* 83, (2011).
- [3] Y. Ando, Topological Insulator Materials, *J. Phys. Soc. Jpn.* 82, 102001 (2013).
- [4] C. L. Kane and E. J. Mele, Z_2 Topological Order and the Quantum Spin Hall Effect, *Phys. Rev. Lett.* 95, 146802 (2005).
- [5] B. A. Bernevig and S.-C. Zhang, Quantum Spin Hall Effect, *Phys. Rev. Lett.* 96, 106802 (2006).
- [6] F. Schindler, A. M. Cook, M. G. Vergniory, Z. Wang, S. S. P. Parkin, B. A. Bernevig, and T. Neupert, Higher-order topological insulators, *Science Advances* 4, eaat0346 (2018).
- [7] B. Xie, H.-X. Wang, X. Zhang, P. Zhan, J.-H. Jiang, M. Lu, and Y. Chen, Higher-order band topology, *Nat Rev Phys* 3, 520 (2021).
- [8] M. König, S. Wiedmann, C. Brüne, A. Roth, H. Buhmann, L. W. Molenkamp, X.-L. Qi, and S.-C. Zhang, Quantum Spin Hall Insulator State in HgTe Quantum Wells, *Science* 318, 766 (2007).
- [9] Z. Fei, T. Palomaki, S. Wu, W. Zhao, X. Cai, B. Sun, P. Nguyen, J. Finney, X. Xu, and D. H. Cobden, Edge conduction in monolayer WTe₂, *Nature Phys* 13, 7 (2017).
- [10] S. Wu, V. Fatemi, Q. D. Gibson, K. Watanabe, T. Taniguchi, R. J. Cava, and P. Jarillo-Herrero, Observation of the quantum spin Hall effect up to 100 kelvin in a monolayer crystal, *Science* 359, 76 (2018).
- [11] A. Murani et al., Ballistic edge states in Bismuth nanowires revealed by SQUID interferometry, *Nature Communications* 8, ncomms15941 (2017).
- [12] F. Schindler et al., Higher-order topology in bismuth, *Nature Phys* 14, 918 (2018).
- [13] J. Tang et al., Dual quantum spin Hall insulator by density-tuned correlations in TaIrTe₄, *Nature* 628, 515 (2024).
- [14] Bent Weber et al., 2024 roadmap on 2D topological insulators, *J. Phys. Mater.* 7, 022501 (2024).
- [15] J.-J. Zhou, W. Feng, C.-C. Liu, S. Guan, and Y. Yao, Large-Gap Quantum Spin Hall Insulator in Single Layer Bismuth Monobromide Bi₄Br₄, *Nano Lett.* 14, 4767 (2014).
- [16] J.-J. Zhou, W. Feng, G.-B. Liu, and Y. Yao, Topological edge states in single- and multi-layer Bi₄Br₄, *New J. Phys.* 17, 015004 (2015).
- [17] C.-H. Hsu, X. Zhou, Q. Ma, N. Gedik, A. Bansil, V. M. Pereira, H. Lin, L. Fu, S.-Y. Xu, and T.-R. Chang, Purely rotational symmetry-protected topological crystalline insulator Bi₄Br₄, *2D Mater.* 6, 031004 (2019).
- [18] F. Tang, H. C. Po, A. Vishwanath, and X. Wan, Efficient topological materials discovery using symmetry indicators, *Nat. Phys.* 15, 470 (2019).
- [19] C. Yoon, C.-C. Liu, H. Min, and F. Zhang, Quasi-One-Dimensional Higher-Order Topological Insulators, arXiv:2005.14710.
- [20] K.-S. Lin et al., Spin-resolved topology and partial axion angles in three-dimensional insulators, *Nat Commun* 15, 550 (2024).
- [21] J. Han, W. Xiao, and Y. Yao, Quasi-one-dimensional topological material Bi₄X₄ (X = Br, I), *Adv. Phys. X* 7, 2057234 (2022).
- [22] R. Noguchi et al., Evidence for a higher-order topological insulator in a three-dimensional material built from van der Waals stacking of bismuth-halide chains, *Nature Materials* 1 (2021).
- [23] Yang, M. et al. Large-Gap Quantum Spin Hall State and Temperature-Induced Lifshitz Transition in Bi₄Br₄. *ACS Nano* 16, 3036–3044 (2022).
- [24] Zhong, J. et al. Coalescence of multiple topological orders in quasi-one-dimensional bismuth halide chains. *Nat Commun* 16, 1163 (2025).
- [25] W. Zhao et al., Topological electronic structure and spin texture of quasi-one-dimensional higher-order topological insulator Bi₄Br₄, *Nat Commun* 14, 8089 (2023).
- [26] J. Han et al., Optical bulk-boundary dichotomy in a quantum spin Hall insulator, *Science Bulletin* 68, 417 (2023).
- [27] N. Shumiya et al., Evidence of a room-temperature quantum spin Hall edge state in a higher-order topological insulator, *Nat. Mater.* 1 (2022).
- [28] J. K. Hofmann et al., Shear-Resistant Topology in Quasi One-Dimensional van Der Waals Material Bi₄Br₄, *Phys. Rev. B* 111, 245415 (2025).
- [29] Peng, X. et al. Observation of Topological Edge States on α Bi₄Br₄ Nanowires Grown on TiSe₂ Substrates. *J. Phys. Chem. Lett.* 12, 10465–10471 (2021).
- [30] D.-Y. Chen, D. Ma, J. Duan, D. Chen, H. Liu, J. Han, and Y. Yao, Quantum transport evidence of boundary states and Lifshitz transition in Bi₄Br₄, *Phys. Rev. B* 106, 075206 (2022).
- [31] H. von Benda, A. Simon, and W. Bauhofer, Zur Kenntnis von BiBr und BiBr–1, *Zeitschrift für anorganische und allgemeine Chemie* 438, 53 (1978).
- [32] T. G. Filatova, P. V. Gurin, L. Kloo, V. A. Kulbachinskii, A. N. Kuznetsov, V. G. Kytin, M. Lindsjo, and B. A. Popovkin, Electronic structure, galvanomagnetic and magnetic properties of the bismuth subhalides Bi₄I₄ and Bi₄Br₄, *Journal of Solid State Chemistry* 180, 1103 (2007).
- [33] X. Li et al., Pressure-induced phase transitions and superconductivity in a quasi-1-dimensional topological crystalline insulator α -Bi₄Br₄, *PNAS* 116, 17696 (2019).
- [34] Z. Gong et al., Br-Vacancies Induced Variable Ranging Hopping Conduction in High-Order Topological Insulator Bi₄Br₄, *Small Methods*, 2400517 (2024).

- [35] J. Zhong, M. Yang, F. Ye, C. Liu, J. Wang, J. Wang, W. Hao, J. Zhuang, and Y. Du, Facet-dependent Electronic Quantum Diffusion in the High-Order Topological Insulator Bi_4Br_4 , *Phys. Rev. Applied* 17, 064017 (2022).
- [36] Zhong, J. et al. Observation of Anomalous Planar Hall Effect Induced by One-Dimensional Weak Antilocalization. *ACS Nano* 18, 4343–4351 (2024).
- [37] L. Qiao et al., Ultralong Single-Crystal $\alpha\text{-Bi}_4\text{Br}_4$ Nanobelts with a High Current Carrying Capacity by Mechanical Exfoliation, *J. Phys. Chem. C* 125, 22312 (2021).
- [38] S.-L. Wu, Z.-H. Ren, Y.-Q. Zhang, Y.-K. Li, J.-F. Han, J.-X. Duan, Z.-W. Wang, C.-Z. Li, and Y.-G. Yao, Gate-tunable transport in van der Waals topological insulator Bi_4Br_4 nanobelts, *J. Phys.: Condens. Matter* 35, 234001 (2023).
- [39] M. S. Hossain et al., Quantum transport response of topological hinge modes, *Nat. Phys.* 1 (2024).
- [40] R. Noguchi et al., A weak topological insulator state in quasi-one-dimensional bismuth iodide, *Nature (London)* 566, 518 (2019).
- [41] See Supplemental Material for a discussion of the crystalline quality of Bi_4Br_4 flakes, resistance networks of two other samples at different temperatures, the length dependence of resistance for samples \mathcal{L} and \mathcal{L}_2 , extended data and analysis on the temperature dependence of the Aharonov-Bohm effect, details of the numerical simulations presented in the main text, the fitting of the magnetoconductance using the formula for 1D weak antilocalization, a presentation of zero-bias anomaly data and comparison with theoretical predictions, and finally extended data on the absence of Hall effect and Shubnikov de Haas oscillations. The Supplemental Material includes Refs [42–62].
- [42] G.-L. Ingold and Y. V. Nazarov, Charge Tunneling Rates in Ultrasmall Junctions, in: "Single Charge Tunneling", edited by H. Grabert and M. H. Devoret, NATO ASI Series B, Vol. 294, pp. 21-107 (Plenum Press, New York, 1992).
- [43] M. H. Devoret, D. Esteve, H. Grabert, G.-L. Ingold, H. Pothier, and C. Urbina, Effect of the electromagnetic environment on the Coulomb blockade in ultrasmall tunnel junctions, *Phys. Rev. Lett.* 64, 1824 (1990).
- [44] F. D. Parmentier, A. Anthore, S. Jezouin, H. le Sueur, U. Gennser, A. Cavanna, D. Mailly, and F. Pierre, Strong back-action of a linear circuit on a single electronic quantum channel, *Nature Phys* 7, 935 (2011).
- [45] M. Bockrath, D. H. Cobden, J. Liu, A. G. Rinzler, R. E. S. L. Balents, and P. L. McEuen, Luttinger-liquid behaviour in carbon nanotubes, *Nature* 397, 598 (1999).
- [46] B. Gao, A. Komnik, R. Egger, D. C. Glatzli, and A. Bachthold, Evidence for Luttinger-Liquid Behavior in Crossed Metallic Single-Wall Nanotubes, *Phys. Rev. Lett.* 92, 216804 (2004).
- [47] C. L. Kane and M. P. A. Fisher, Transport in a one-channel Luttinger liquid, *Phys. Rev. Lett.* 68, 1220 (1992).
- [48] C.-H. Hsu, P. Stano, J. Klinovaja, and D. Loss, Helical liquids in semiconductors. *Semicond. Sci. Technol.* 36, 123003 (2021).
- [49] T. Li et al., Observation of a Helical Luttinger Liquid in InAs/GaSb Quantum Spin Hall Edges, *Phys. Rev. Lett.* 115, 136804 (2015).
- [50] R. Stühler, F. Reis, T. Müller, T. Helbig, T. Schwemmer, R. Thomale, J. Schäfer, and R. Claessen, Tomonaga-Luttinger liquid in the edge channels of a quantum spin Hall insulator, *Nat. Phys.* 16, 47 (2020).
- [51] A. Q. Wang et al., A robust and tunable Luttinger liquid in correlated edge of transition-metal second-order topological insulator $\text{Ta}_2\text{Pd}_3\text{Te}_5$, *Nat. Commun.* 14, 7647 (2023).
- [52] D. S. Golubev and A. D. Zaikin, Coulomb Interaction and Quantum Transport through a Coherent Scatterer, *Phys. Rev. Lett.* 86, 4887 (2001).
- [53] A. L. Yeyati, A. Martin-Rodero, D. Esteve, and C. Urbina, Direct Link between Coulomb Blockade and Shot Noise in a Quantum-Coherent Structure, *Phys. Rev. Lett.* 87, 046802 (2001).
- [54] M. Kindermann and Yu. V. Nazarov, Interaction Effects on Counting Statistics and the Transmission Distribution, *Phys. Rev. Lett.* 91, 136802 (2003).
- [55] I. Safi and H. Saleur, One-Channel Conductor in an Ohmic Environment: Mapping to a Tomonaga-Luttinger Liquid and Full Counting Statistics, *Phys. Rev. Lett.* 93, 126602 (2004).
- [56] D. S. Golubev, A. V. Galaktionov, and A. D. Zaikin, Electron transport and current fluctuations in short coherent conductors, *Phys. Rev. B* 72, 205417 (2005).
- [57] B. L. Al'tshuler and D. E. Khmel'nitskii, Fluctuation properties of small conductors, *Pis'ma Zh. Eksp. Tear. Fiz.* 42, 291 (1985) [*JETP Lett.* 42, 359 (1985)].
- [58] D. E. Khmel'nitskii and A. I. Larkin, Nonlinear conductance in the mesoscopic regime, *Phys. Scr. T14*, 4 (1986).
- [59] R. A. Webb, S. Washburn, and C. P. Umbach, Experimental study of nonlinear conductance in small metallic samples, *Phys. Rev. B* 37, 8455 (1988).
- [60] H. Tang and Y. Fu, Intrinsic nonlinear conductance of mesoscopic conductors, *Phys. Rev. Lett.* 67, 485 (1991).
- [61] W. G. van der Wiel, Yu. V. Nazarov, S. De Franceschi, T. Fujisawa, J. M. Elzerman, E. W. G. M. Huizeling, S. Tarucha, and L. P. Kouwenhoven, Electromagnetic Aharonov-Bohm effect in a two-dimensional electron gas ring, *Phys. Rev. B* 67, 033307 (2003).
- [62] Y. Yamauchi et al., Universality of bias- and temperature-induced dephasing in ballistic electronic interferometers, *Phys. Rev. B* 79, 161306 (2009).
- [63] R.B. Bapat, Resistance matrix of a weighted graph, *MATCH Commun. Math. Comput. Chem* 50, 73-82 (2004).
- [64] Devriendt Karel, Graph Geometry from Effective Resistances, PhD Thesis, Trinity College, 2022.
- [65] Datta, S. *Electronic Transport in Mesoscopic Systems*. (Cambridge Univ. Press, Cambridge, 2009).
- [66] This method of finding the conductance matrix can only be applied if describing the sample as a network of resistors is adequate, meaning that the transport between nodes is reciprocal.
- [67] E. Akkermans and G. Montambaux, *Mesoscopic Physics of Electrons and Photons*, Cambridge University Press (2007).
- [68] S. Hikami, A. I. Larkin, and Y. Nagaoka, Spin-Orbit Interaction and Magnetoresistance in the Two Dimensional Random System, *Progress of Theoretical Physics* 63, 707 (1980).
- [69] H. Steinberg, J.-B. Laloë, V. Fatemi, J. S. Moodera, and P. Jarillo-Herrero, Electrically tunable surface-to-bulk coherent coupling in topological insulator thin films,

- Phys. Rev. B 84, 233101 (2011).
- [70] J. Chen, X. Y. He, K. H. Wu, Z. Q. Ji, L. Lu, J. R. Shi, J. H. Smet, and Y. Q. Li, Tunable surface conductivity in Bi_2Se_3 revealed in diffusive electron transport, Phys. Rev. B 83, 241304 (2011).
- [71] P. A. Lee, A. D. Stone, and H. Fukuyama, Universal conductance fluctuations in metals: Effects of finite temperature, interactions, and magnetic field, Phys. Rev. B 35, 1039 (1987).
- [72] P. Mohanty and R. A. Webb, High-Field Measurements of Electron Decoherence Time in Metallic Nanowires: Switching off Magnetic Impurity Spins, Phys. Rev. Lett. 91, 066604 (2003).
- [73] C. W. J. Beenakker and H. Van Houten, Flux-cancellation effect on narrow-channel magnetoresistance fluctuations, Phys. Rev. B 37, 6544 (1988).
- [74] Groth, C. W., Wimmer, M., Akhmerov, A. R. and Waintal, X. Kwant: a software package for quantum transport. New J. Phys. 16, 063065 (2014).
- [75] M. Büttiker, Absence of backscattering in the quantum Hall effect in multiprobe conductors, Phys. Rev. B 38, 9375 (1988).
- [76] M. Büttiker, Symmetry of electrical conduction, IBM J. Res. Dev. 32, 317 (1988).
- [77] B. Gao, Y. F. Chen, M. S. Fuhrer, D. C. Glattli, and A. Bachtold, Four-Point Resistance of Individual Single-Wall Carbon Nanotubes, Phys. Rev. Lett. 95, 196802 (2005).
- [78] G. Timp, A. M. Chang, P. Mankiewich, R. Behringer, J. E. Cunningham, T. Y. Chang, and R. E. Howard, Quantum transport in an electron-wave guide, Phys. Rev. Lett. 59, 732 (1987).
- [79] de Picciotto, R., Stormer, H. L., Pfeiffer, L. N., Baldwin, K. W. and West, K. W. Four-terminal resistance of a ballistic quantum wire. Nature 411, 51–54 (2001).
- [80] S. Washburn and R. A. Webb, Aharonov-Bohm effect in normal metal quantum coherence and transport, Advances in Physics 35, 375 (1986).
- [81] Dufouleur, J. et al. Quasiballistic Transport of Dirac Fermions in a Bi_2Se_3 Nanowire. Phys. Rev. Lett. 110, 186806 (2013).
- [82] Jauregui, L. A., Pettes, M. T., Rokhinson, L. P., Shi, L. and Chen, Y. P. Magnetic field-induced helical mode and topological transitions in a topological insulator nanoribbon. Nature Nanotech 11, 345–351 (2016).
- [83] G. Behner et al., Aharonov-Bohm Interference and Phase-Coherent Surface-State Transport in Topological Insulator Rings, Nano Lett. 23, 6347 (2023).
- [84] Pan, Z.-C. et al. Altshuler-Aronov-Spivak interference of one-dimensional helical edge states in MoTe_2 . Phys. Rev. B 107, 045411 (2023).
- [85] A. E. Hansen, A. Kristensen, S. Pedersen, C. B. Sørensen, and P. E. Lindelof, Mesoscopic decoherence in Aharonov-Bohm rings, Phys. Rev. B 64, 045327 (2001).
- [86] J. Lefeuvre et al, Quantum Coherent Transport of 1D Ballistic States in Second Order Topological Insulator Bi_4Br_4 , Zenodo (2025), 10.5281/zenodo.17953562.

Supplemental material : Quantum Coherent Transport of 1D Ballistic States in Second Order Topological Insulator Bi_4Br_4

Jules Lefeuvre,^{1,*} Masaru Kobayashi,² Gilles Patriarche,³ Nathaniel Findling,³ David Troadec,⁴ Meydi Ferrier,¹ Sophie Guéron,¹ Hélène Bouchiat,¹ Takao Sasagawa,² and Richard Deblock^{1,†}

¹*Université Paris-Saclay, CNRS, Laboratoire de Physique des Solides, 91405, Orsay, France.*

²*Materials and Structures Laboratory, Institute of Science Tokyo, Yokohama, Japan.*

³*Université Paris-Saclay, CNRS, Centre de Nanosciences et de Nanotechnologies, 91120, Palaiseau, France.*

⁴*Université de Lille, CNRS, Institut d'Electronique, de Microélectronique et de Nanotechnologie, 59652, Villeneuve d'Ascq, France*

This part provides supplementary information for the article "Quantum Coherent Transport of 1D ballistic states in second order topological insulator Bi_4Br_4 ". The following topics are discussed: the crystalline quality of Bi_4Br_4 flakes, resistance networks of two other samples at different temperatures, the length dependence of resistance for samples \mathcal{L} and \mathcal{L}_2 , extended data and analysis on the temperature dependence of the Aharonov-Bohm effect, details of the numerical simulations presented in the main text, the fitting of the magnetoconductance using the formula for 1D weak anti-localization, a presentation of zero-bias anomaly data and comparison with theoretical predictions, and finally extended data on the absence of Hall effect and Shubnikov de Haas oscillations.

I. CRYSTAL QUALITY AND CONTACT REGION

As a reference, we assess the disorder in pristine exfoliated flakes before any contact is made. To this end, we exfoliate Bi_4Br_4 in a glove box using bare PDMS stamps. The Bi_4Br_4 -covered stamps are brought into contact with a silicon wafer piece previously spin-coated with PMMA 950 A3. The chip is then pressed onto a Transmission Electron Microscope (TEM) copper grid (of size 1500 mesh), which sticks to the PMMA. It is then briefly taken outside the glove box to dissolve the PMMA in an acetone bath, thus separating the TEM grid from the wafer piece. This procedure results in the deposition of Bi_4Br_4 flakes onto the TEM grid, some of which bridge across the holes (Fig.S1a), making them suitable for observation. Images of several flakes revealed excellent crystalline quality, despite an exposure to ambient air of approximately one hour. An example is shown in (Fig.S1b and c), where the flake is aligned along the a direction. Strikingly, the flake maintains its crystalline order up to the outermost layers.

The FIB cross-section of the contact regions have been observed and analyzed in a STEM (Microscope FEI ThermoFisher TEM/STEM Titan Themis 200). The areas under the contacts of samples with contacts on top show significant damage to the crystal structure of Bi_4Br_4 , and the elemental maps reveal an increase in bismuth and palladium content, with a simultaneous decrease in bromine content directly below the gold (Fig. 1e of the main text). We attribute the degradation of Bi_4Br_4 into amorphous Bi to the IBE step before contact deposition, which causes interdiffusion of Bi in the thin layer of Pd deposited on top. The damaged areas

can extend to several tens of nanometers away from the contacts.

Even in the absence of a disorder-inducing step such as IBE, ohmic contacts made on Bi_4Br_4 are invasive. Indeed, we present STEM-EDX elemental maps on samples with contacts below the flakes (Fig. 1 f,g of the main text). The STEM images reveal that this method does not result in a uniform interface between the flake and the Pd track. The flake is separated from the contact by a nearly continuous 3 nm-thick layer, pierced by asperities of the Pd electrodes, thereby permitting an electrical contact with the flake. Further inspection of this layer reveal that it is rich in silicon and carbon, hinting towards residues of uncrosslinked-PDMS which seem to cover nearly all of our Bi_4Br_4 flakes. This thin layer of residue likely comes from the exfoliation process, and may contribute to the relatively long stability in air that we have observed in our samples.

It is interesting to note that the regions in which the residue layer has been pierced by Pd show Bi_4Br_4 crystal damage similar to that of the evaporated contacts. Amorphous regions show up to 25 % of Pd and 65 % Bi, indicating a diffusion of the palladium from the contacts into the crystal over several tens of nanometers. This interdiffusion process is somewhat anisotropic : the diffusion regions are generally less than 20 nm deep and extend laterally about 100nm.

II. CONDUCTANCE MATRIX FOR SAMPLES \mathcal{H}_2 AND \mathcal{H}_3

We present the conductance matrices measured on two extra samples, \mathcal{H}_2 and \mathcal{H}_3 measured at 4 K and 300 K respectively. For all samples the resistance values we find are all in the $\text{k}\Omega$ range (see main text and Fig S2). These conductance matrices confirm the anisotropy discussed in the main text.

* jules.lefeuvre@universite-paris-saclay.fr

† richard.deblock@universite-paris-saclay.fr

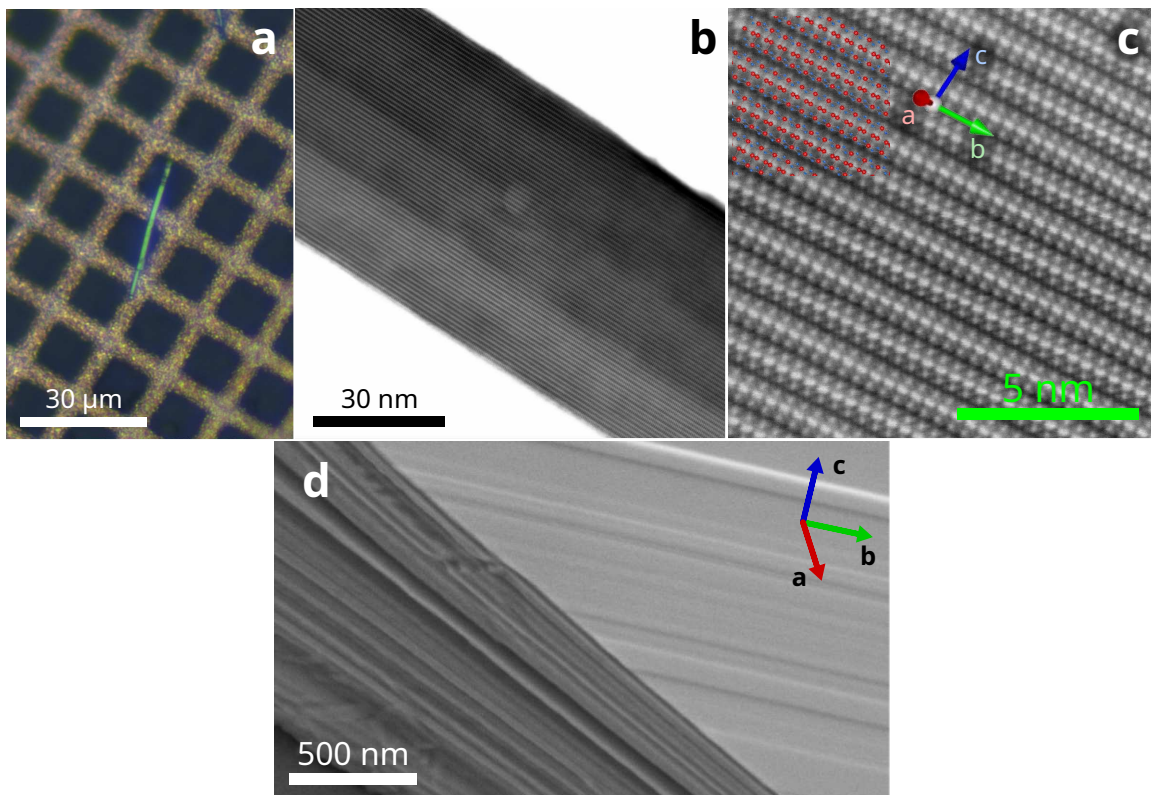


FIG. S1. a) Optical picture of an exfoliated Bi_4Br_4 ribbon on a TEM grid. b) Bright Field STEM image of the flake. c) Atomic resolution HAADF-STEM image revealing alignment of the atomic columns near the a axis. On the top-left the atomic model of Bi_4Br_4 is superimposed to the STEM image. d) SEM image of a typical Bi_4Br_4 flake showing a striated top surface.

III. RESISTANCE AND LENGTH DEPENDENCE OF SAMPLE \mathcal{L} AND \mathcal{L}_2

A. Length dependence of resistance for sample \mathcal{L}

We present the data for two Bi_4Br_4 samples ; \mathcal{L} is contacted by Pd(7 nm)/Au(100 nm) electrodes onto a doped silicon substrate, which serves as a back gate, covered by 500 nm of oxide and \mathcal{L}_2 , which was stamped onto 20 nm thick palladium electrodes. Both were measured in a dilution fridge with a base temperature of around 10 mK. Sample \mathcal{L} (Fig S5 of main text) has five segments, ranging from 1 μm to 5 μm , and \mathcal{L}_2 has segments of length 200 nm to 1 μm , which resistances are reported in tables III A and III A respectively. For both samples, the resistance of the segments do not increase linearly with their lengths, which indicates that they are dominated by a contact resistance.

Length (μm)	1	2	3	4	5
R (k Ω)	1.6	3.2	2.8	5.5	2.7

TABLE I. Length and resistance of the different segments of sample \mathcal{L} .

Length (nm)	200	300	400	500	600	700	800	900	1000
R (k Ω)	5.02	1.86	2.01	1.36	1.56	2.05	1.91	0.96	5.98

TABLE II. Length and resistance of the different segments of sample \mathcal{L}_2 .

B. Gate and field dependence of conductance fluctuations

As presented in the main text, sample \mathcal{L} exhibits conductance fluctuations at low temperatures as a function of magnetic field. We found that these fluctuations also exist as a function of gate voltage, with a similar amplitude, as expected from the ergodic nature of UCF (Fig. S3).

IV. AHARONOV-BOHM EFFECT OF SAMPLES \mathcal{H}_1 AND \mathcal{L}

The resistance of sample \mathcal{H}_1 exhibits AB oscillations. The period of these oscillations does not depend on temperature but the amplitude does (Fig. S4) and leads to the exponential decay discussed in the main text.

The peaks identified on the FFT of the magnetocon-

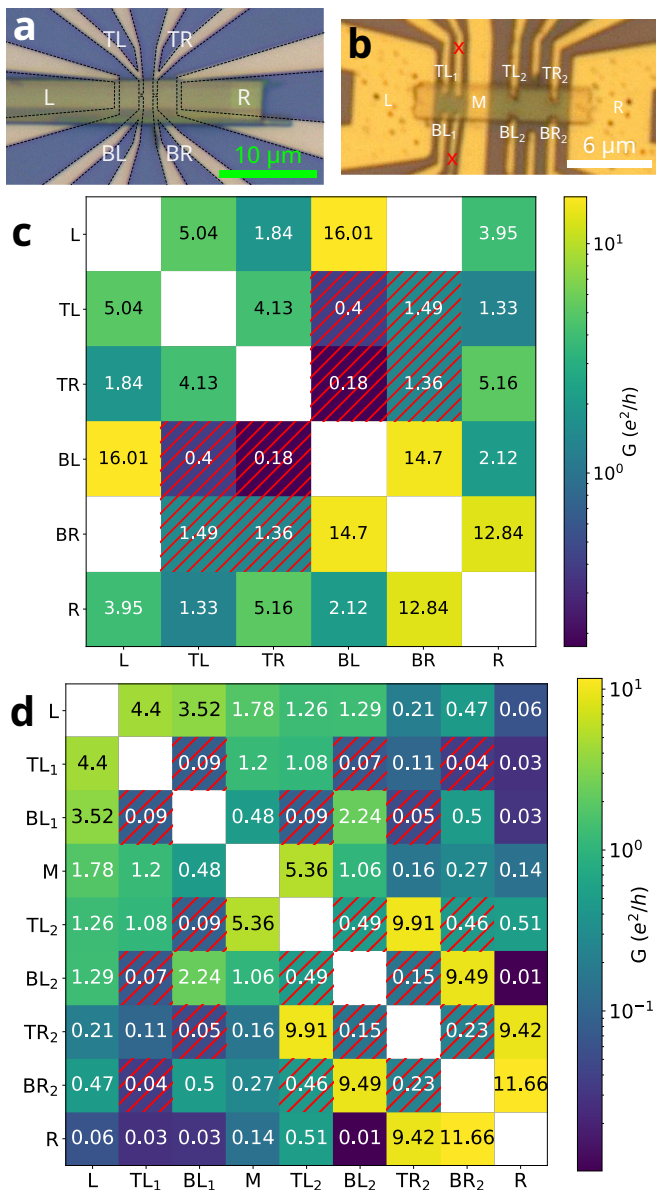


FIG. S2. a) Optical image of sample \mathcal{H}_2 . b) Optical image of sample \mathcal{H}_3 . c) Conductance matrix of sample \mathcal{H}_3 taken at 300 K. d) Conductance matrix of sample \mathcal{H}_2 taken at 4 K. For both matrices, transverse conductances are hatched in red.

ductance of sample \mathcal{L} , denoted α , β , γ and δ (Fig. 9b and c of the main text), can be associated to different locations of the edge states. These locations corresponds to relatively simple stackings of a few Bi_4Br_4 unit cells (Inset of Fig. S5), yielding reasonable agreement between the measured and expected values for the magnetic frequency rescaled to a $1\mu\text{m}$ segment $f_B^{1\mu\text{m}}$ (Table III). For the γ peak, the large difference in height (7.9 nm) between the edge states in the proposed stack allows it to be tested with a transverse magnetic field in the range achievable with our vector magnet. The corresponding experimental data is shown in Fig. S6 and indeed exhibits a consistent peak in the Fourier transform at the

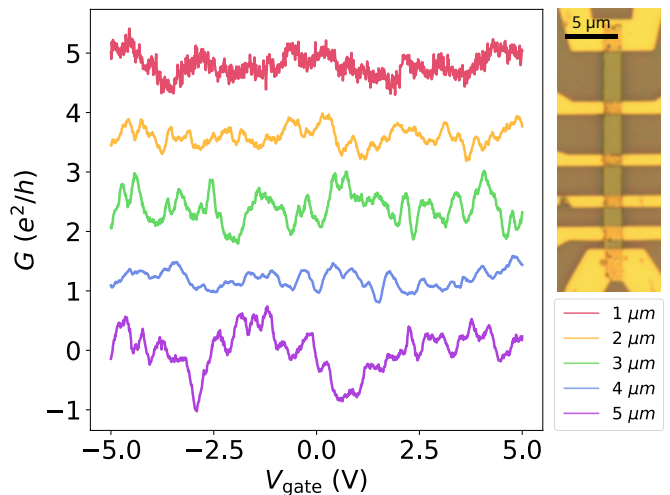


FIG. S3. Gate dependence of the conductance at 10 mK for all segments of sample \mathcal{L} . The mean value is subtracted and the curves are shifted for clarity. Right : optical picture of sample \mathcal{L} .

expected magnetic frequency ($f_B/L=1.92\text{T}^{-1}$).

As for the temperature dependence of sample \mathcal{H}_1 , we find an exponential decay with temperature for a majority of identified AB peaks in the FFT of all segments of sample \mathcal{L} . This dependence is calculated by measuring the area under an identified peak (α , β , γ and δ , and their harmonics) as a function of temperature. Fitting of this area to ae^{-bT} is done for the first harmonic, the n^{th} harmonics are allowed only a 5% adjustment around a/n and $b \times n$, which gives a reasonable agreement for a smaller set of peaks. This exponential decay is consistent with a $1/T$ dependence of the phase coherence length and a value of this length at 1K between 1.5 and $6\mu\text{m}$, of the same order of magnitude than the scale obtained on sample \mathcal{H}_1 .

Peak label	α	β	γ	δ
$f_B^{1\mu\text{m}}$ (T^{-1})	0.61	0.77	1	1.4
W_{meas}^z (nm)	2.5	3.2	4.1	5.8
W_{th}^z (nm)	2.61	3.23	4.07	5.84
W_{th}^y (nm)	0	2.6	7.9	2.6

TABLE III. Modelization of the measured magnetic frequencies $\alpha - \gamma$ in the Fourier transform of sample \mathcal{L} with simple stackings of a few Bi_4Br_4 unit cells (Fig. S5). For each peaks the measured magnetic frequency $f_B^{1\mu\text{m}}$, the corresponding width W_{meas}^z and the associated horizontal (W_{th}^z) and vertical (W_{th}^y) distance are given.

Sample \mathcal{H}_1 has proven to be quite sensitive to small current spikes, that seem to have modified its disorder each time it has happened. As a consequence, we have selected only a few curves to show in the main text.

First, we take a look at the reproducibility of AB oscil-

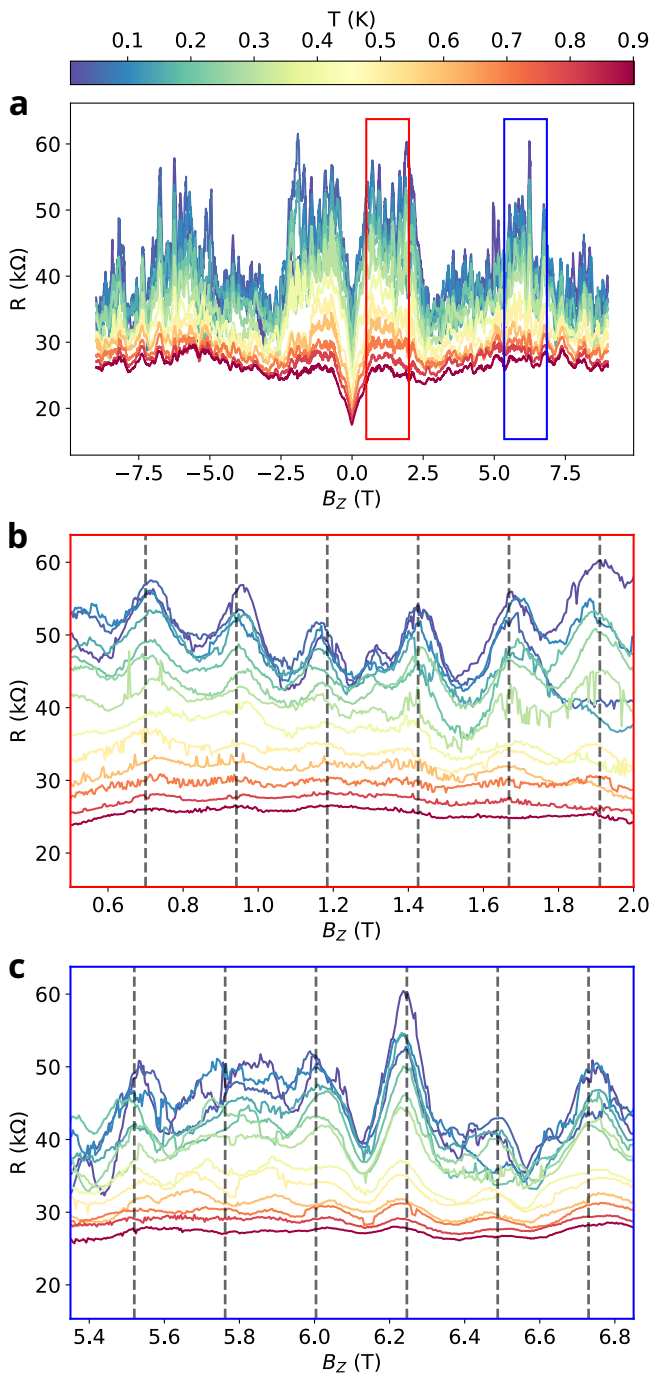


FIG. S4. a) Magnetoresistance of sample \mathcal{H}_1 at different temperatures from 10 mK to 900 mK, indicated by the color scale. b) and c) show two reduced magnetic ranges, indicated by the red and blue rectangles on a). The data show that the period of AB oscillations does not depend on temperature, but that their amplitude decreases rapidly with temperature.

lation with variations in disorder. We show five curves, corresponding to three disorder realizations and different current biases. We can first notice a strong reduction of the AB amplitude when increasing the AC current from 1 nA to 10 nA. This seems to be linked to the nonlinear-

ity of the conductance of Bi_4Br_4 sections, as discussed in the section "Zero bias anomaly". Hence, we stuck to 1 nA current bias to get the maximum AB amplitude. Nevertheless, all of our data show a pronounced peak in Fourier space $f_B = 4.16 \text{ T}^{-1}$, indicating its intrinsic nature. Because the study of AB oscillations with varying temperature was only done for configuration **C**, it is the data shown in the main text.

Then, we examine the consistence of the observed negative 4-wire resistance. We see that all of the longitudinal magnetoresistance traces taken with the two top electrodes exhibit negative values in some field ranges. However, we could not benefit from the increased AB amplitude at lower biases, due to spurious time-dependent telegraphic noise hindering the repeatability of our data at 1 nA. Interestingly, the four-wire resistance measured with the two bottom electrodes (not shown) does not exhibit excursions to negative values. This may be explained by a difference in invasiveness between the two sets of electrodes ; the two-wire resistance through the top electrodes is $\sim 130 \text{ k}\Omega$, while it is $\sim 35 \text{ k}\Omega$ for the bottom ones.

V. NUMERICAL SIMULATION OF THE UCF AND AB EFFECT OF BALLISTIC CHANNELS

Transport simulations shown on figure 8 of the main text were made using Kwant Python package [1]. We have simulated ballistic wires (200x3 sites) between two diffusive regions (50x100 sites) on a square lattice of parameter a (see insets of Fig. 8), with one orbital and no spin degree of freedom, using the following tight-binding Hamiltonian :

$$\hat{\mathbf{H}} = \sum_i (4t + D_{\text{rand}}) a_i^\dagger a_i + \sum_{\langle i,j \rangle} t_{ij}(\phi) a_i^\dagger a_j \quad (1)$$

The onsite Hamiltonian has an added disorder term D_{rand} which equals 0 in the ballistic wires, and follow a uniform random distribution over $[-D, D]$ elsewhere. The out-of-plane magnetic field is incorporated in the hopping term using the Peierls substitution, with :

$$t_{ij}(\phi) = -t \exp(-i\phi(x_i - x_j)(y_i + y_j)/2) \quad (2)$$

The simulation shown in the main text were made using the following parameters : $a = 1$, $t = 1$, $D = 1$, $\phi \in [-0.05; 0.05]$, $E = 1.8$. We simulate two geometries. The first one is a single ballistic wire between two diffusive regions, which exhibits conductance fluctuations (Fig. 8a of the main text). The second configuration corresponds to two ballistic wires. In this case the conductance exhibits AB oscillation with a field scale determined by a flux quantum in the area enclosed by the two wires (Fig. 8b of the main text).

The question arises as to whether trajectories in the region of diffusive contacts could blur the Aharonov-Bohm effect. This is for example what is seen in AB ring with

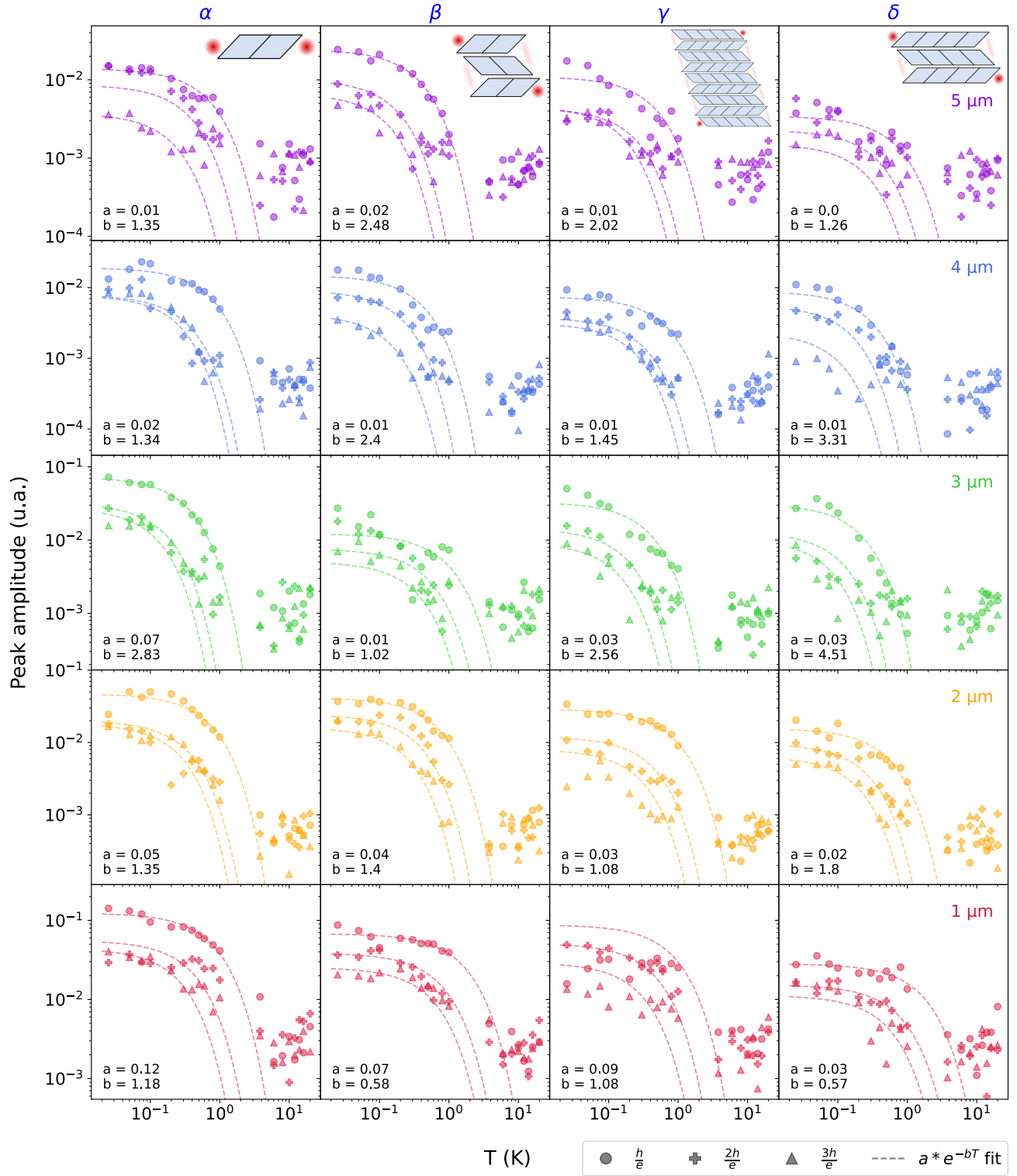


FIG. S5. Temperature dependence of the peak amplitude of the Fourier transform corresponding to AB effect in the conductance fluctuations of sample \mathcal{L} for all segments. For each segment and for each family of peak (α , β , γ and δ), the first (circle), second (cross) and third (triangle) harmonics are fitted using an exponential decay. Fitting to $a e^{-bT}$ is done for the first harmonic, the n^{th} harmonics are allowed only a 5% adjustment around a/n and $b \times n$. The reference fit is done on the second harmonic of γ for the $1 \mu\text{m}$ section. Insets : stacking picture of the cross-section of the sample surface, consistent with the considered peak, where a blue diamond represents a crystalline unit cell and the red dots the position of edge states compatible with the observed AB periodicity.

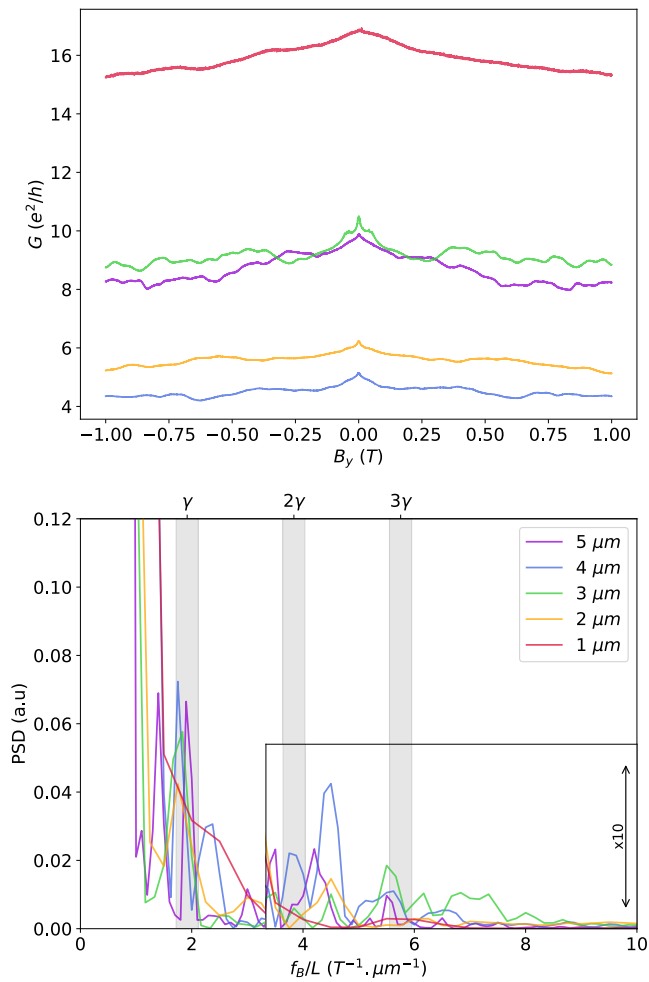


FIG. S6. Aharonov-Bohm oscillations in \mathcal{L} with in-plane transverse magnetic field. **a)** Magnetoconductances of each segment at 10 mK. **b)** Power spectral density of the magnetoconductance signals with FFT frequencies rescaled by the length of each segment. Peaks corresponding to the expected in-plane response of γ are highlighted. The PSD amplitude is multiplied by 10 at higher f_B for better visibility of the peaks.

low aspect ratio (large width compared to perimeter). However we find on the contrary that the AB effect, especially for sample H1 (Fig. 7 of the main text) has a relatively well defined magnetic field period that seems in contradiction with the previous point. We think that this good visibility of the AB oscillations is due to the fact that the interfering 1D edge states are separated by a distance of the order of the mean free path of the diffusive region. In this limit the two paths cannot be considered independently in a quasi-classical picture and lead to relatively well define AB oscillations. When the separation of the edge states is much higher than the mean free path, the contribution from different trajectories in the region of diffusive contacts leads to a strong decrease of the visibility of the oscillation. We have conducted numerical simulations using Kwant package to support this

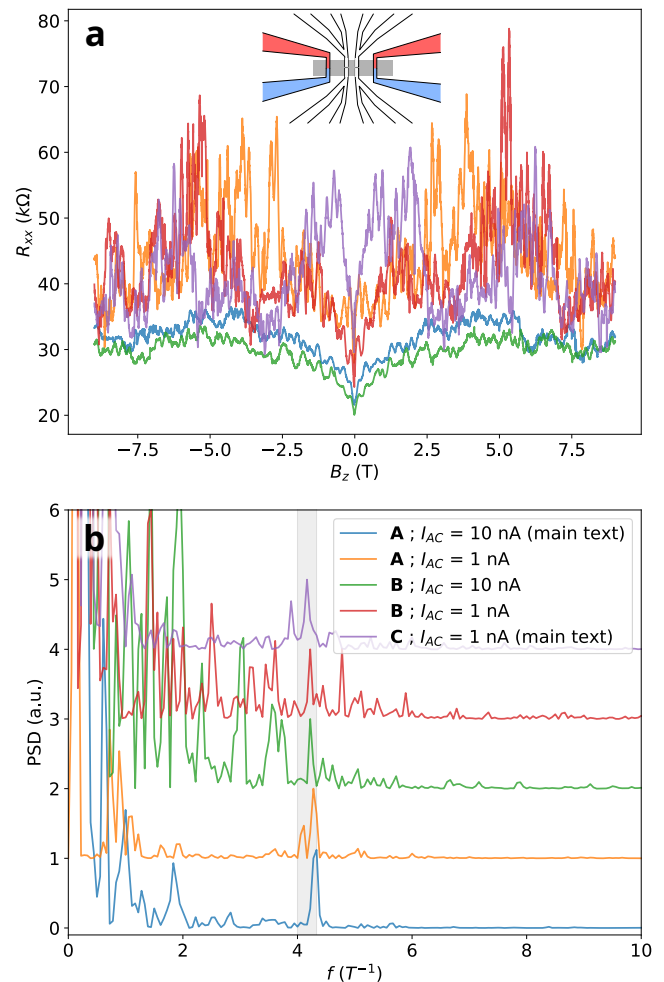


FIG. S7. a) Magnetoresistance curves of sample \mathcal{H}_1 for different disorder configurations and (**A**, **B** and **C**) and current biases (1 nA or 10 nA). b) PSDs of all magnetoresistance curves, normalized by their values at $f_B = 4.16 \text{ T}^{-1}$. Despite differences in disorder realizations, all measurements show a peak in their Fourier transform corresponding to AB oscillations of period 0.24 T.

point. For this we have considered two 1D ballistic states separated by a distance W and contacted to two diffusive coherent contacts (100x100 sites, disorder=2.0). We have calculated the conductance as a function of magnetic field for separation varying between 10 and 70 lattice steps (Fig. S9). With the chosen disorder strength w and energy E the mean free path $l_e = 48a\sqrt{E}/t(t/w)^2$ is estimated to 16 lattice sites. We find that the amplitude of the AB effect is relatively high for separation of the order of l_e . However when the separation is higher than several l_e the AB effect is much less visible. This expected blurring of the AB oscillations should occur in rings connected with constrictions, but such experiments likewise show well-defined magnetic field periodicities [27, 28].

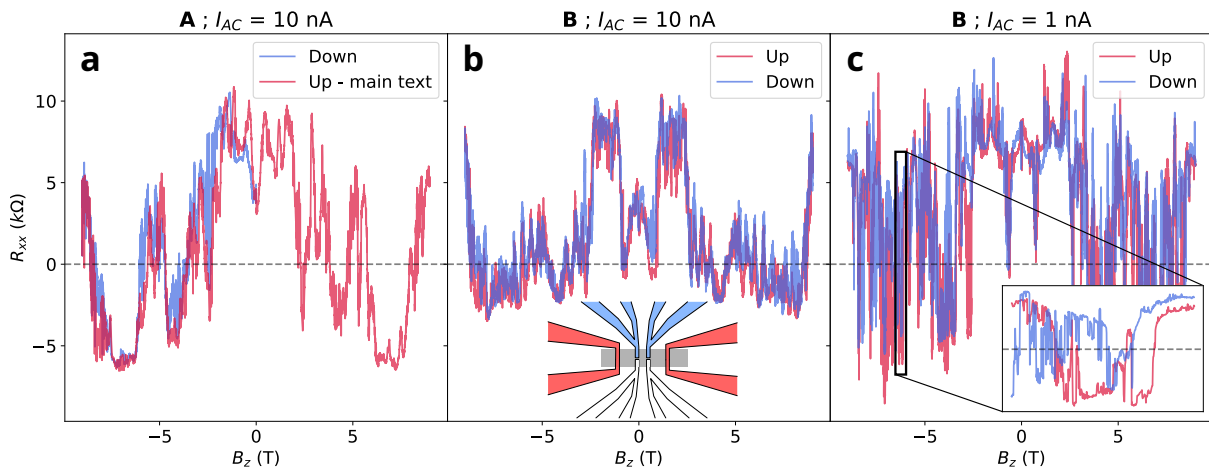


FIG. S8. Reproducibility of the negative 4-wire resistance for sample \mathcal{H}_1 . **A** (panel a) and **B** (panels b) and c) denote two disorder realizations, before and after a power cut. a) and b) are magnetoresistance curves taken with 10 nA AC current polarization, whereas c) was taken with 1 nA AC polarization. While a) and b) show decent repeatability between up and down field sweeps, c) shows significant telegraphic noise in certain field regions.

VI. FITTING OF MAGNETO CONDUCTANCE WITH 1D WEAK ANTI-LOCALIZATION

We have tried to fit the magnetoconductance of sample \mathcal{L} with the formula describing weak anti-localization for quasi-1D geometry using formula :

$$\delta G(B) = \frac{\alpha e^2}{2hL} \left(\frac{1}{l_\varphi^2} + \frac{e^2 B^2 W^2}{3\hbar^2} \right)^{-1/2} \quad (3)$$

with l_φ the phase coherence length, L the length of the sample, W its width, B the magnetic field and α a prefactor corresponding to the number of independent channels [2]. The fitted data are shown on figure S10.

Assuming that the length L is the one of the considered segment, one obtains fit parameters listed in Table IV. The parameters are not consistent and vary a lot from segment to segment.

TABLE IV. Fit parameters using 1D WAL for sample \mathcal{L} .

Length (μm)	α	l_φ (nm)	W (nm)	G_0 (e^2/h)
5	20.9	586	13.6	7.33
4	37.7	116	76	3.87
3	12.8	878	4	7.43
2	20	153	22	4.28
1	1.1	2429	6	14.76

VII. ZERO BIAS ANOMALY

The features (WAL, UCF and AB effect) described in the main text of the article concern the linear regime of

quantum transport. When applying a DC current bias through the sample, added to the small ac current (typically in the nA range) used to probe the differential resistance, this latter quantity exhibits a peak around zero voltage (Fig. S11a). This is a universal characteristic for all our samples, even if the amplitude and width of the peak vary from sample to sample. The zero bias anomaly (ZBA) has been reported in very different systems spanning from tunnel junctions [3, 4] or quantum point contacts [5] in a resistive environment to transport in 1D systems as carbon nanotubes [6, 7], edge states of quantum spin hall [10, 11, 26] or second order topological insulator [12] and are either attributed to Coulomb interaction affecting quantum transport or Tomonaga Luttinger Liquid (TLL) physics [8, 9]. Both effect can lead to power law dependence of ZBA [16, 18] and scaling behaviour but from different physical origin. Whereas the energy scale for DCB is determined by the charging energy E_C of the conductor and the exponent α by the impedance of the electromagnetic environment and of the sample [3, 13–15, 17, 18], the TLL model cutoff is given by the Thouless energy $\hbar v_F/L$ of the 1D conductor of length L and Fermi velocity v_F and the exponent $\alpha = (K + K^{-1} - 2)/2$ by the interaction parameter K .

The TLL scenario is appealing because of the expected 1D nature of the edge states in Bi_4Br_4 . However, for sample \mathcal{L} , with section length L varying from 1 to $5\mu\text{m}$ and v_F around 5.10^5m.s^{-1} [23–25] one expects a power law behaviour for T higher than a cutoff temperature $\hbar v_F/(k_B L)$ [8] between 0.8 and 3.8K. As a consequence we can exclude the TLL scenario since in all our samples, we have seen the ZBA disappear around 2K. Moreover this scenario should lead to a systematic variation with the length of the sample, which is not seen in the experiment.

Another possibility is that quantum transport is af-

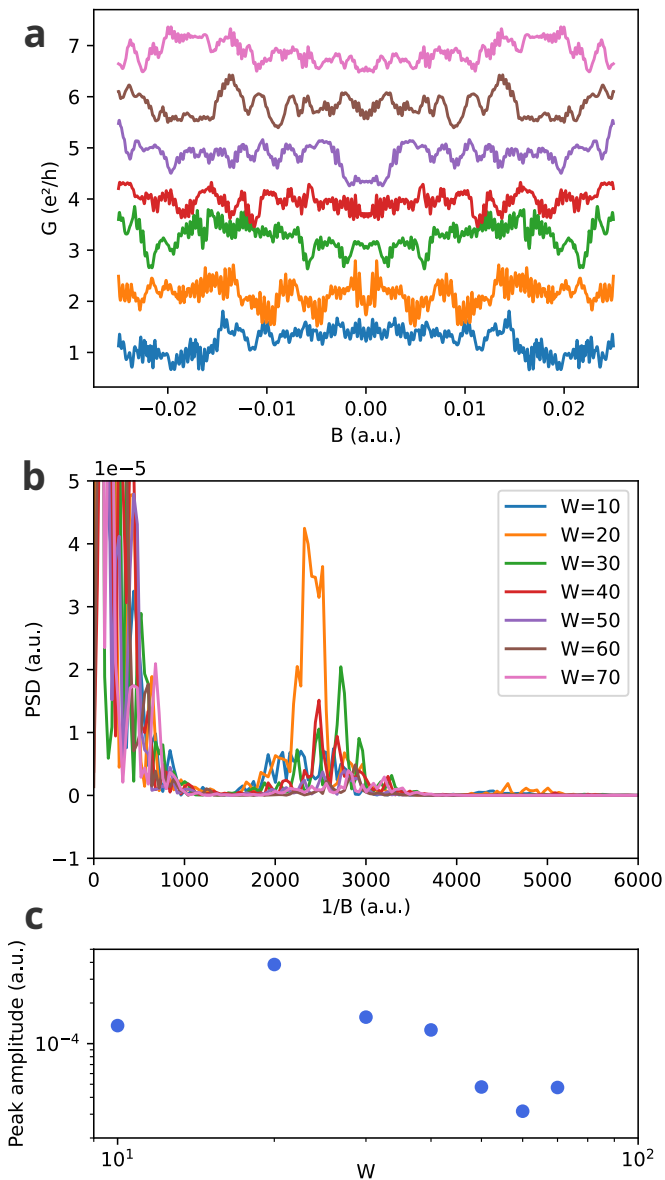


FIG. S9. Simulation of the AB effect for different separation W of ballistic edge states. The length L of the ballistic channels is adjusted so as to keep the same periodicity of the AB effect. a) Magnetoconductance for different widths. The colors correspond to legend of b. (b) FFT of the magnetoconductance. (c) Amplitude of the FFT peak integrated between 1200 and 3700 for the different widths.

ected by Coulomb interaction. In this picture we assume that the samples can be described by several coherent conducting channels in parallel, and that the transport of each channel is affected by the back-action of the other channels. We note that if each channel is perfectly ballistic no effect of the electromagnetic environment should exist. However due to the existence of small diffusive coherent region between the contact and the Bi_4Br_4 crystal, we rather assume, based on results discussed in the main text of the article, that the samples are well described by imperfectly transmitted coherent channels, the transmis-

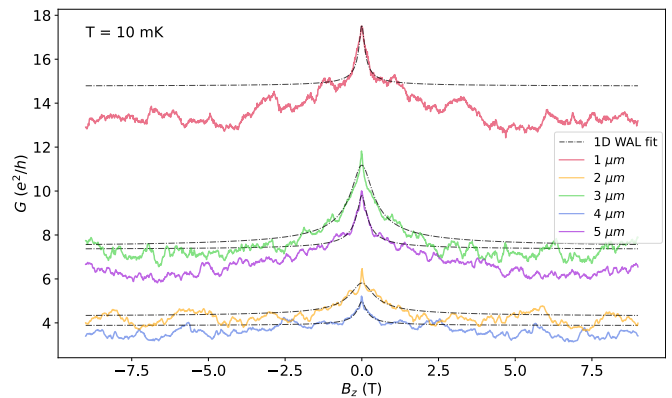


FIG. S10. Fit of the magnetoconductance using formula 3 for quasi-1D geometry. The quality of the fit is not very good and lead to non consistent parameters.

sion of which can be modulated by quantum interference effects. In this situation, Coulomb interaction leads to an energy dependence of the transmission coefficient and thus to ZBA [3, 13–17]. We apply the results for Coulomb blockade in a coherent conductor due to its own resistance [13] and use in particular the relation giving the current voltage characteristic of the conductor:

$$I = G_0 V - \frac{e\beta k_B T}{\hbar} \text{Im} \left[w\Psi \left(1 + \frac{w}{2} \right) - iv\Psi \left(1 + i\frac{v}{2} \right) \right] \quad (4)$$

with $w = u + iv$, $u = \hbar G_0 E_C / (e^2 \pi^2 k_B T)$, $v = eV / (\pi k_B T)$ and Ψ the digamma function. In this equation the adjustable parameters are G_0 , the conductance of the sample without interaction effect, β , an effective Fano factor which is associated with the transmission of the conductor considered and gives the amplitude of the effect at very low temperature, and E_C the charging energy.

Figure S11b shows the fitted curves for the 3 μm long segment of sample \mathcal{L} at different temperatures. We give in table VII the fitted parameters for each segment.

Length (μm)	E_C (meV)	β	G_0 (e^2/h)
1	0.041	0.52	19.59
2	0.155	0.33	10.62
3	0.020	0.99	13.90
4	0.196	0.23	6.72
5	0.99	0.10	11.41

TABLE V. Length and ZBA fit parameters (see text) for the different segments of sample \mathcal{L} .

This agreement is only consistent for temperatures higher than 80 mK, that we attribute to a saturation of electronic temperature below this limit. We note however that formula 4 cannot explain the peaks in dI/dV seen in the longer segment (Fig. S11a). We postulate

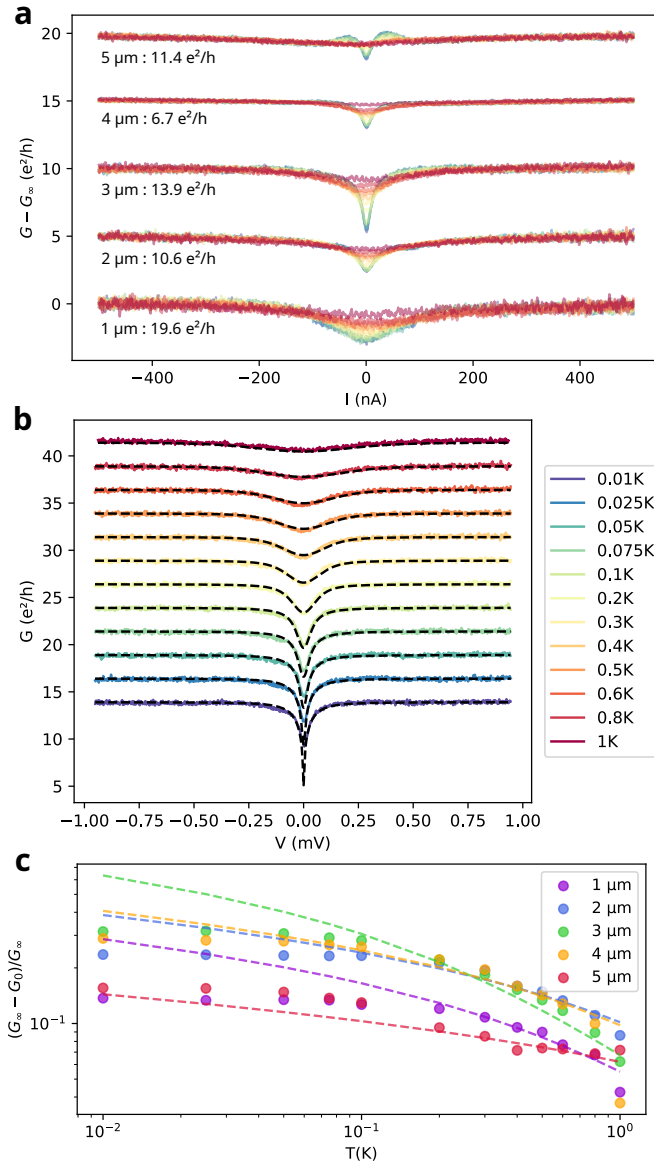


FIG. S11. a) Differential conductance of the different segments of sample \mathcal{L} as a function of DC current, for temperatures indicated by the legend of b. The length of the considered segment is indicated together with the high bias conductance G_0 . The curves are shifted for clarity. b) Differential conductance dI/dV of the 3 μm segment of sample \mathcal{L} and fit with the prediction of ref. [13] (eq. 25) for temperature indicated by the legend. c) Temperature dependence of the relative amplitude of the zero bias peak. All the peaks exhibit a temperature scale in the Kelvin range. The dashed lines indicates the temperature behaviour expected from the fit based on ref. [13]

that this may be due to the intrinsic energy dependence of the transmission coefficients. Furthermore, the relatively high dispersion of the parameters we obtain for the different segments calls for a better understanding of this non-linear effect.

In parallel with the ZBA, coherent effects disappear

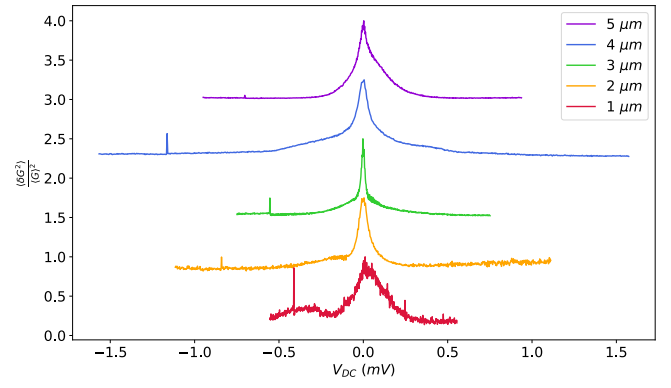


FIG. S12. Ratio of the amplitude of the conductance fluctuation, deduced from the gate voltage dependence of the conductance, and conductance squared for the different segments of sample \mathcal{L} . The ratio is normalized by the value at zero bias. The curves are shifted by 0.75 for clarity.

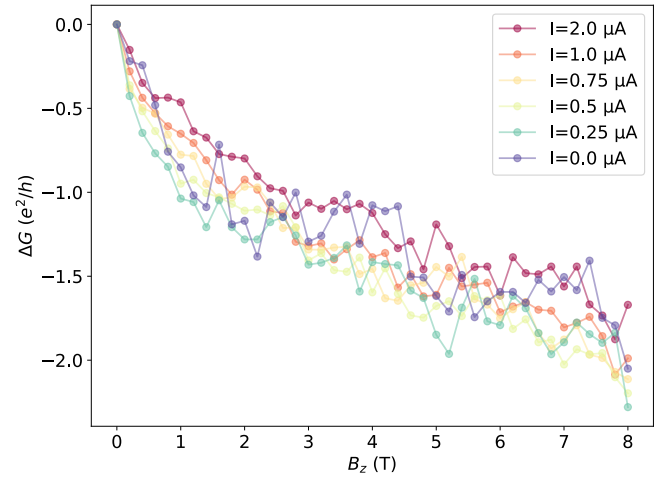


FIG. S13. WAL correction $\Delta G = G(B) - G(B = 0 \text{ T})$ for varying DC current biases at $T = 10 \text{ mK}$.

at finite current. This affects the conductance fluctuation on a voltage scale of the order of 50 μeV (deduced from half width at half maximum), with no clear correlation with the length of the section considered (Fig. S12). However the WAL correction is not affected by a finite bias (Fig. S13). This rules out thermal effects and self-heating that would otherwise affects both UCF and WAL through the temperature dependence of the phase coherence length. The energy scale affecting the amplitude of the UCF is expected to be related to the Thouless energy in diffusive coherent sample [19–21] but can involve also the mean level spacing [22]. In our case the Thouless energy E_{th}^{1D} of the 1D helical states $\hbar v_F/L$ gives an energy scale between 330 μeV for the shorter section and 66 μeV for the longer one, taking $v_F = 5 \cdot 10^5 \text{ m.s}^{-1}$. This is not consistent with the voltage scale measured especially because of the absence of correlation with the length of the sample. The Thouless

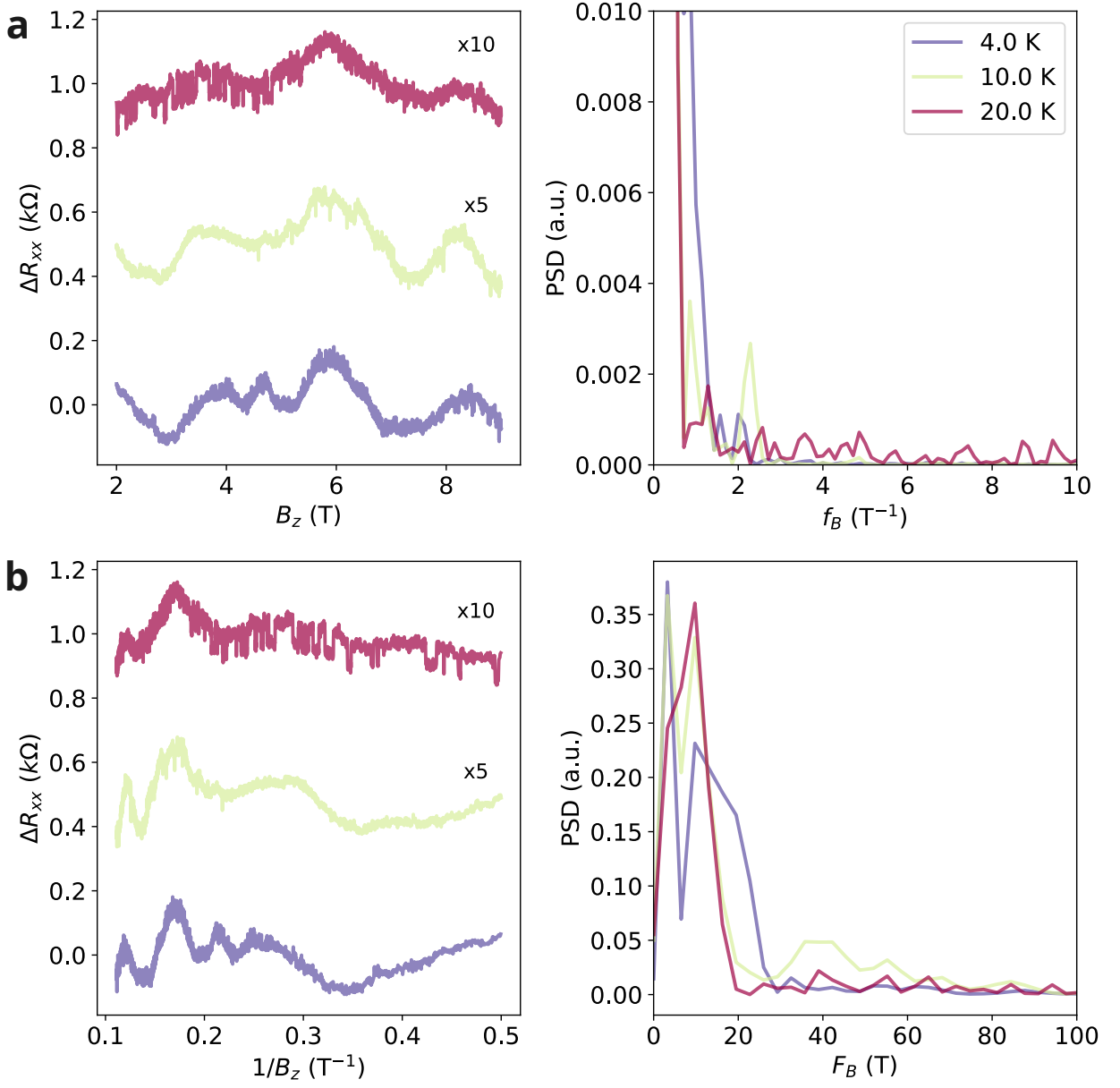


FIG. S14. a) Left: 4-wire longitudinal resistance of sample \mathcal{H}_1 as a function of out-of-plane magnetic field B_z at temperatures 4 K, 10 K and 20 K (indicated by legend). A linear baseline has been removed, curves have been shifted by 500 Ω for clarity, and data at 10 K and 20 K are multiplied by a factor shown in the figure. Right : power spectral density (PSD) of the same data, showing no particular periodicity in the signal, as expected for the UCFs. b) Same data plotted as a function of $1/B_z$. No specific periodicity appears in the direct signal or PSD.

energy E_{th}^D of the diffusive coherent contact can be estimated $E_{th}^{diff} = \hbar D/L_D^2$ using $D = v_F^D l_e^D/3$ where we take reasonable values for the unknown Fermi velocity of the Bi/Pd alloy $v_F^D = 10^6$ m.s $^{-1}$ and its mean free path $l_e^D = 5$ nm, leading to $E_{th}^D = 110$ μ eV for a length L_D of the diffusive region of 100 nm. So it seems that the measured voltage scale of the UCF decrease is more consistent with the one imposed by the coherent diffusive region.

VIII. ABSENCE OF HALL EFFECT OR SHUBNIKOV DE HAAS OSCILLATIONS

As detailed in section 3 of the main text, sample \mathcal{H}_1 does not show any Hall effect. This is consistent with the very strong anisotropy of electronic transport in this sample, which together suggest the absence of bulk and (001) surface conduction. Figure S14 shows the magnetoresistance of the same sample for temperatures between 4 K and 20 K as a function of out-of-plane magnetic field B_z and $1/B_z$ for a field greater than 2 T and the cor-

responding power spectral density. This analysis shows that the conductance fluctuations has no specific period-

icity as expected for UCFs, thus are not consistent with Shubnikov-de Haas oscillations nor Aharonov-Bohm oscillations.

-
- [1] C. W. Groth, M. Wimmer, A. R. Akhmerov, X. Waintal, Kwant: a software package for quantum transport, *New J. Phys.* 16, 063065 (2014).
- [2] E. Akkermans and G. Montambaux, *Mesoscopic Physics of Electrons and Photons*, Cambridge University Press (2007).
- [3] G.-L. Ingold and Y. V. Nazarov, Charge Tunneling Rates in Ultrasmall Junctions, in: "Single Charge Tunneling", edited by H. Grabert and M. H. Devoret, NATO ASI Series B, Vol. 294, pp. 21-107 (Plenum Press, New York, 1992).
- [4] M. H. Devoret, D. Esteve, H. Grabert, G.-L. Ingold, H. Pothier, and C. Urbina, Effect of the electromagnetic environment on the Coulomb blockade in ultrasmall tunnel junctions, *Phys. Rev. Lett.* 64, 1824 (1990).
- [5] F. D. Parmentier, A. Anthore, S. Jezouin, H. le Sueur, U. Gennser, A. Cavanna, D. Mailly, and F. Pierre, Strong back-action of a linear circuit on a single electronic quantum channel, *Nature Phys* 7, 935 (2011).
- [6] M. Bockrath, D. H. Cobden, J. Liu, A. G. Rinzler, R. E. S. L. Balents, and P. L. McEuen, Luttinger-liquid behaviour in carbon nanotubes, *Nature* 397, 598 (1999).
- [7] B. Gao, A. Komnik, R. Egger, D. C. Glatzli, and A. Bachtold, Evidence for Luttinger-Liquid Behavior in Crossed Metallic Single-Wall Nanotubes, *Phys. Rev. Lett.* 92, 216804 (2004).
- [8] C. L. Kane and M. P. A. Fisher, Transport in a one-channel Luttinger liquid, *Phys. Rev. Lett.* 68, 1220 (1992).
- [9] C.-H. Hsu, P. Stano, J. Klinovaja, and D. Loss, Helical liquids in semiconductors. *Semicond. Sci. Technol.* 36, 123003 (2021).
- [10] T. Li et al., Observation of a Helical Luttinger Liquid in InAs/GaSb Quantum Spin Hall Edges, *Phys. Rev. Lett.* 115, 136804 (2015).
- [11] R. Stühler, F. Reis, T. Müller, T. Helbig, T. Schwemmer, R. Thomale, J. Schäfer, and R. Claessen, Tomonaga-Luttinger liquid in the edge channels of a quantum spin Hall insulator, *Nat. Phys.* 16, 47 (2020).
- [12] A. Wang et al., A robust and tunable Luttinger liquid in correlated edge of transition-metal second-order topological insulator Ta₂Pd₃Te₅, *Nat Commun* 14, 1 (2023).
- [13] D. S. Golubev and A. D. Zaikin, Coulomb Interaction and Quantum Transport through a Coherent Scatterer, *Phys. Rev. Lett.* 86, 4887 (2001).
- [14] A. L. Yeyati, A. Martin-Rodero, D. Esteve, and C. Urbina, Direct Link between Coulomb Blockade and Shot Noise in a Quantum-Coherent Structure, *Phys. Rev. Lett.* 87, 046802 (2001).
- [15] M. Kindermann and Yu. V. Nazarov, Interaction Effects on Counting Statistics and the Transmission Distribution, *Phys. Rev. Lett.* 91, 136802 (2003).
- [16] I. Safi and H. Saleur, One-Channel Conductor in an Ohmic Environment: Mapping to a Tomonaga-Luttinger Liquid and Full Counting Statistics, *Phys. Rev. Lett.* 93, 126602 (2004).
- [17] D. S. Golubev, A. V. Galaktionov, and A. D. Zaikin, Electron transport and current fluctuations in short coherent conductors, *Phys. Rev. B* 72, 205417 (2005).
- [18] The exponent α of the power law dependence is the Dynamical blockade regime depends on the regime of parameters considered. For a small tunnel junction of very high impedance in a resistive environment of impedance R one gets $\alpha = -2/g$, with $g = R_K/R$ and $R_K = h/e^2$ the resistance quantum [3]. For a coherent conductor of resistance R_S in the same situation and in the limit of weak back-scattering, $\alpha = -2/(g+g_S)$ with $g_S = R_K/R_S$ [17].
- [19] B. L. Al'tshuler and D. E. Khmel'nitskii, *Pis'ma Zh. Eksp. Tear. Fiz.* 42, 291 (1985) [*JETP Lett.* 42,359(1985)]
- [20] D. E. Khmel'nitskii and A. I. Larkin, Nonlinear Conductance in the Mesoscopic Regime, *Phys. Scr.* T14, 4 (1986).
- [21] R. A. Webb, S. Washburn, and C. P. Umbach, Experimental study of nonlinear conductance in small metallic samples, *Phys. Rev. B* 37, 8455 (1988).
- [22] H. Tang and Y. Fu, Intrinsic nonlinear conductance of mesoscopic conductors, *Phys. Rev. Lett.* 67, 485 (1991).
- [23] J.-J. Zhou, W. Feng, G.-B. Liu, and Y. Yao, Topological edge states in single- and multi-layer Bi₄Br₄, *New J. Phys.* 17, 015004 (2015).
- [24] C. Yoon, C.-C. Liu, H. Min, and F. Zhang, Quasi-One-Dimensional Higher-Order Topological Insulators, arXiv:2005.14710 [*Cond-Mat*] (2020).
- [25] N. Shumiya et al., Evidence of a room-temperature quantum spin Hall edge state in a higher-order topological insulator, *Nat. Mater.* 1 (2022).
- [26] Z. Fei, T. Palomaki, S. Wu, W. Zhao, X. Cai, B. Sun, P. Nguyen, J. Finney, X. Xu, and D. H. Cobden, Edge conduction in monolayer WTe₂, *Nature Phys* 13, 7 (2017).
- [27] W. G. van der Wiel, Yu. V. Nazarov, S. De Franceschi, T. Fujisawa, J. M. Elzerman, E. W. G. M. Huizeling, S. Tarucha, and L. P. Kouwenhoven, Electromagnetic Aharonov-Bohm effect in a two-dimensional electron gas ring, *Phys. Rev. B* 67, 033307 (2003).
- [28] Y. Yamauchi et al, Universality of bias- and temperature-induced dephasing in ballistic electronic interferometers, *Phys. Rev. B* 79, 161306 (2009).